



Eidgenössische Technische Hochschule Zürich
Swiss Federal Institute of Technology Zurich

Identifying Limiting Noise Sources in a Cryogenic Ion-Trap System

Master's Thesis

Aida Mashaal

Supervisors:

Dr. Christopher Axline
Prof. Dr. Jonathan Home

November 23, 2022

Acknowledgements

First and foremost, I would like to thank Prof. Jonathan Home for supporting me throughout my Master's program at ETH and allowing me to conduct a semester and master's thesis in the TIQI group. I would also like to thank my supervisor, Chris Axline, for taking the time to meet with me weekly and guiding me through tough times. Finally, I am grateful for everyone else in the TIQI group who took joy in helping me with various questions and troubles.

Abstract

Heating rates are an essential metric in the performance of ion-trap systems in quantum computing [1]. Motional heating of the ion limits the fidelity of quantum operations. External noise sources play an important role in heating the ion and, to a greater extent, in cryogenic ion-trap systems. Identifying external noise sources is, therefore, pivotal for improving the heating rates of ion trap systems.

This thesis develops a method for modeling heating rates of external noise sources in a cryogenic ion-trap setup at the Trapped Ion Quantum Information group in ETH Zurich. The method relies on experimental noise measurements and electronic simulations. Noise sources were modeled generically, and empirical metrics were developed to help identify sources. The dominant noise source for this system was thereby identified, and the system's grounding configuration proved to be most limiting. Attempts to reduce the noise through several modified grounding configurations were successful, with heating rates lowered by almost an order of magnitude.

Contents

Acknowledgements	i
Abstract	ii
1 Introduction	1
2 Heating Rates	3
2.1 Possible Noise Sources	5
2.1.1 Surface Effects	5
2.1.2 External Sources	5
2.2 Measurement Techniques	8
2.2.1 Sideband Spectroscopy	8
2.2.2 Carrier Slowdown Method	9
2.2.3 Doppler Recooling	10
3 Ion Trap Setups	11
3.1 Traps	11
3.1.1 Dragonfly Trap	11
3.1.2 PIEDMONS Trap	11
3.2 Surrounding Environment	13
3.2.1 Cryogenic System	13
3.2.2 Voltage Lines	15
3.2.3 Grounding	18
4 Technical Concepts and Appropriate Devices	20
4.1 Noise Spectral Density	20
4.1.1 Resolution- vs Noise Equivalent- Bandwidth	21
4.2 Noise Propagation	22
4.3 Device Comparison for Noise Measurements	23

5	Modeling External Noise Sources: PIEDMONS Trap	27
5.1	Measured Heating Rates	27
5.2	DC Circuit Noise	29
5.2.1	Source Characterization	32
5.3	RF Circuit Noise	34
5.3.1	SS vs Cu cable	36
5.4	Electromagnetic Pickup Noise	36
5.5	Noise in the Dragonfly Trap	38
6	Noise Models	41
6.1	Independent vs Common Mode Noise	41
6.2	Noise Polarization Ratio	42
7	Modifications and Recent Heating Rates	45
7.1	Measured Heating Rates vs. Setup Configurations	45
8	Conclusion and Outlook	49
	Bibliography	52

Introduction

The 2022 Physics Noble Prize was awarded to Alain Aspect, John F. Clauser, and Anton Zeilinger for experimentally establishing the existence of the quantum phenomenon known as entanglement. Erwin Schrödinger referred to entanglement as not “one but ‘the’ characteristic trait of quantum mechanics”. The pioneering work by the laureates supported quantum mechanics and laid the foundation for the emerging field of quantum computing. Trapped ions provide a prime example of the importance of entanglement through its application in quantum computing.

Alexei Kitaev proved that a set of multiple single-qubit operations and one two-qubit operation could efficiently simulate any quantum circuit [2]. Trapped-ion quantum computers use the relatively long lifetimes of the ion’s internal states of the ion for encoding quantum information. Single-ion operations use coherent light interactions to manipulate the internal states of the ion [3]. In contrast, two-qubit operations require entanglement of the internal states of the ion to its motion [4, 5]. Yet, although the physical implementation of one- [6–9] and two-ion experiments [10, 11] has been demonstrated, achieving a high fidelity of operations such that quantum error correction can be performed is rather challenging. Due to internal and motional state entanglement, the fidelity of two-qubit operations on ions is dominantly limited by the ion’s motional heating on the operation’s timescales [3]. This so-called ‘heating’ of the ion is understood to be the mechanism where the motional state of the ion is environmentally perturbed by electric-field noise and uncontrollably acquires additional quanta, or phonons [?]. This type of heating is problematic as it leads to decoherence of the quantum information encoded in the ion. Characterization of ion-trap systems, therefore, places a large emphasis on the system’s heating rates. Many studies have been dedicated to understanding the mechanism of the heating rates and how to improve them.

Ions are typically confined in space through a combination of electric fields. An essential requirement of ion traps is a high-quality vacuum to prevent the loss of ions through background gas collisions. Initially, ion trap experiments took place in ultra-high vacuum setups at room temperature. Achieving an ultra-high vacuum is challenging and requires the ion-trap system to be baked at 200°C. This

process requires at least two to three weeks and must be repeated each time the system is opened. The downtime of experiments due to system baking motivated the use of cryogenic apparatuses, which can reach an ultra-high vacuum within hours. At the same time, observations of improved heating rates at cryogenic temperatures caused a surge of interest in cryogenic ion-trap systems [12]. Many ion-trap systems today, especially small traps for scalable trapped ion quantum computing, are cooled to cryogenic temperatures.

Yet the benefit of cryogenic temperatures on heating rates is more complicated than it seems. Cryogenic temperatures benefit heating rates if the heating source is due to trap-related effects. This noise source is typically deemed “anomalous” due to its unknown origins and has been of great interest to surface science research [13]. But despite those benefits, the complexity of cryogenic setups relative to room temperature setups raises concerns for external noise sources, which are often overlooked in ion-trap systems. For instance, cryogenic setups require much longer signal paths ($\gtrsim 50$ cm) due to thermalization requirements. These sources can originate in the electronics or the environment surrounding the ion trap. Within the Trapped Ion Quantum Information group at ETH Zurich, several cryogenic setups present high heating rates on the same order of magnitude ($\sim 10^2 - 10^3$). These setups host different-sized traps and have been speculated to be limited by external noise sources. In this thesis, we attempt to identify the noise sources leading to such heating rates for the PIEDMONS [14] trap setup by comparing theoretical models to measured heating rates on the ion. Moreover, we will compare a similar setup, which hosts the Dragonfly trap [15], in terms of dominating noise sources and heating rates. Results allow us to draw general conclusions on noise behavior in cryogenic ion-trap systems.

The thesis is structured as follows: **Chapter 2** introduces heating rates, reviews possible heating sources in general ion-trap systems, and lists heating rate measurement techniques on the ion. **Chapter 3** will introduce the PIEDMONS and the Dragonfly traps and their respective experimental setups. In **Chapter 4**, technical and mathematical concepts required for noise measurements will be discussed. **Chapter 5** will model expected noise sources in the PIEDMONS trap and compare them with measured heating rates to find the dominant noise source. A similar analysis of the Dragonfly will be discussed. In **Chapter 6**, we investigate the noise correlation of different electrodes and the effect on the heating rates of the ions. Based on the dominating noise source, **Chapter 7** will describe setup modifications and subsequently measured heating rates on the ion. Lastly, **Chapter 8** summarizes the main results, lists additional setup modifications, and discusses their possible effects on heating rates.

Heating Rates

Linear Paul traps use a combination of static (DC) and oscillating radiofrequency (RF) fields to confine the ion in three dimensions (3D). The oscillating RF voltages generate confinement in the radial direction through a pseudopotential approximation. In this approximation, the ion's motion consists of large-scale oscillations at a frequency known as the trap frequency, ω_t and superimposed on small-scale oscillation, known as micromotion, at the RF drive frequency, Ω_{RF} . Under minimization of micromotion [16, 17], the ion motion can approximately be described as a harmonic oscillator [18]. Apart from the electric fields used for trapping, stray electric fields from the environment could couple to the ion's motion, causing excitation. The rate at which the motional state acquires additional quanta is the heating rate.

A trapped ion's sensitivity to small electric field fluctuations can be attributed to its electric dipole moment [18]. Close to the ground state, the electric dipole moment is given by $d_{DM} \approx qa_0$, where $a_0 = \sqrt{\hbar/2m\omega_t}$ the extent of the ground state wave function and m the ion's mass. With typical trap frequencies around $\omega_t = 2\pi \times 1$ MHz this amounts to $a_0 \approx 10$ nm. Assuming a one-dimensional treatment of the motion, the Hamiltonian in the presence of an external fluctuating electric field $\Phi(t, x)$ is given by [18]

$$\hat{H}(t) = \hat{H}_0(t) + q\Phi(t, \mathbf{r}_I) - qE(t)\hat{x} + \dots, \quad (2.1)$$

where $\hat{H}_0(t)$ is the bare trapping potential, $E(t) = -\mathbf{e}_t \cdot \nabla\Phi(t, r_I)$ is the electric field component at the position of the ion \mathbf{r}_I along a mode of interest \mathbf{e}_t , and $\Phi(t, r_I)$ is a global potential offset which does not contribute to the motion of the ion. Moving to the interaction picture with respect to $\hat{H}_0(t)$, the Hamiltonian becomes

$$\hat{H}(t)_{coupling} = -qE(t)\hat{x}. \quad (2.2)$$

Our interest lies in the overall effect of fluctuations rather than a single instance in time; hence we average out the noisy electric field in our calculations. If we suppose the ion starts in the motional ground state $|0\rangle$, we can predict the

rate at which the ion is excited into the first vibrational state $|1\rangle$ using first-order perturbation theory. This is given by

$$\Gamma_{0\rightarrow 1} = \frac{q^2}{2\hbar m\omega_t} \int_{-\infty}^{\infty} \langle E(t)E(t+\tau) \rangle_t e^{i\omega_t\tau} d\tau. \quad (2.3)$$

The integral describes the Fourier transform of the auto-correlation function, which is the electric-field noise spectral density, $S_E(\omega_t)$ ¹ with units of $(\text{V}^2/\text{m}^2\text{Hz})$. Generalizing the heating rate as the rate at which the average thermal occupation changes, we obtain

$$\Gamma_h = \dot{n} = \frac{q^2}{4\hbar m\omega_t} S_E(\omega_t). \quad (2.4)$$

Equation (2.4) is most commonly used in literature to describe heating rates in ion-trap systems. It assumes that the ion sits at the trap's center, which should ideally coincide with the RF null [18]. However, a stray electric field could displace the trap's minimum from the RF null such that micromotion becomes non-negligible. Micromotion is not strictly a noise source since it is a periodic modulation of the ion's mean position. Nevertheless, a non-zero electric field component exists away from the RF null. This would mean that noise on the RF electrodes would cause fluctuations at the ion. Dominant noise contributions in the RF circuitry arise at the trap drive frequency Ω_{RF} due to passive band-pass filtering this frequency (see Section 3.2.2). Moreover, the gradient of the noisy electric field couples the displacement of the ion from the RF null with the amplitude of the micromotion, modulating the noise at Ω_{RF} [18]. The additional contributions relative to Equation (2.4) to heating of the ion based on the effects mentioned above are given by²

$$\Gamma_h^{RF,\pm} \approx 4 \frac{q^2}{4\hbar m\omega_t} \left(\frac{q\Phi''_{RF}}{2m\Omega_{RF}^2} \right)^2 \frac{(\Phi''_{RF})^2 S_V(\Omega_{RF} \pm \omega_t) (\Delta x)^2}{V_{RF}^2}, \quad (2.5)$$

where Δx is the displacement from the RF null, Φ''_{RF} is the second derivative of the oscillating RF potential, and V_{RF} is the RF voltage amplitude. The additional terms scale with a prefactor of $(\omega_t/\Omega_{RF})^2$. For typical trap, $\omega_t \sim 2\pi \times 1-3$ MHz, and RF drive frequencies $\Omega_{RF} \sim 2\pi \times 20-50$ MHz, these terms are at least two orders of magnitude smaller than Equation (2.4). Hence, these effects are negligible in the absence of resonances.

¹Single-sided noise spectral density.

²For a detailed derivation see [18].

2.1 Possible Noise Sources

Various studies have been dedicated to understanding the mechanisms of noise coupling into an ion-trap system [13, 19]³. Nevertheless, many ambiguities surround this platform. The main limitation is identifying the exact noise source resulting in the measured heating rates since the ion can only sample the total electric field noise at the operated trap frequency. In the following, we will differentiate between intrinsic noise sources, i.e., trap-related and extrinsic sources, and the different mechanisms through which they contribute to noise in ion-trap systems.

2.1.1 Surface Effects

Several studies provided strong evidence of noise originating from the ion-trap surface itself [13, 20]. This noise is predominantly associated with surface contamination, as studies show reduced heating rates with surface treatment [21]. Although specific models that predict similar scaling of heating rates on ion-electrode distance ($S_E \propto d^{-4}$) have been developed, e.g., fluctuating patch potentials [13], extensive studies of noise vs. temperature and frequency are required to specify the underlying mechanism. As traps become smaller for practical purposes, the ion is trapped closer to the surface and, therefore, is more susceptible to surface noise. Though surface noise proves an obstacle to scaling trapped ion systems, improvements would likely be based on materials involved in the fabrication of the trap electrodes [22], which is out of the scope of this thesis. Moreover, observations lead us to believe that this noise does not yet limit our setups. This will be addressed in more detail in later chapters.

For further references on proposed mechanisms, their frequency scaling, and experimental evidence, see [22].

2.1.2 External Sources

As external noise sources, we consider sources that can introduce noise to the electrodes through the experimental setup. This includes, for instance, noise through the environment or trapping circuitry. We start our consideration of relevant noise sources by looking at **blackbody radiation**, the most fundamental source of noise as every object is subject to such radiation. Freely propagating electromagnetic radiation couple to the ion, causing heating. At typical trap frequencies $\omega_t = 2\pi \times 1$ MHz and for room and cryogenic temperatures, this would result in a noise spectral density of $S_E \sim 10^{-22} - 10^{-24}$ V²/m²Hz, respectively.

³Among other references summarized in [18].

Typical noise spectral densities of different-sized ion-trap systems and their corresponding heating rates at a trap frequency of $\omega_t = 2\pi \times 1$ MHz are shown in Figure 1. The noise spectral density of blackbody radiation is evidently far below typical noise spectral density in ion-trap systems and is mostly neglected.

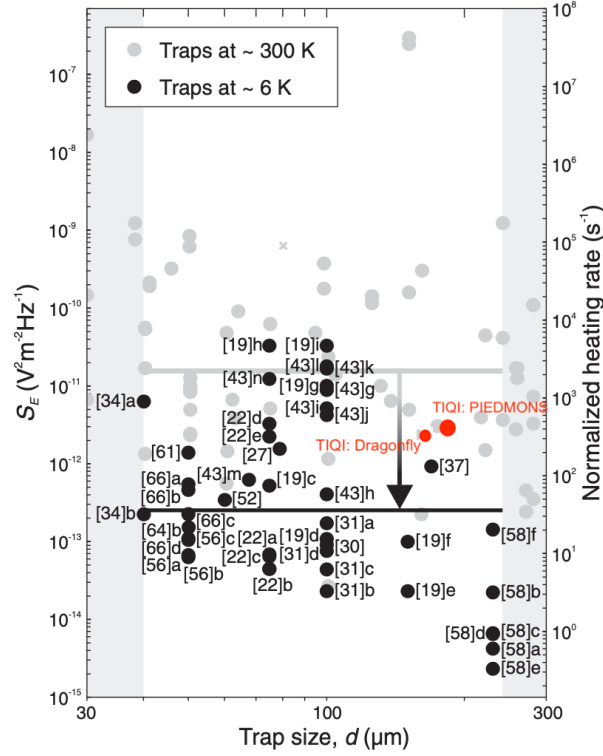


Figure 1: Electric-field noise spectral density S_E as a function of the ion-electrode distance, d . Figure taken from [18], where the square bracket values refer to citations in [18]. Grey and black data points correspond to traps operated at room and cryogenic temperatures, respectively. The normalized heating rates correspond to a trapped $^{40}\text{Ca}^+$ with a motional frequency of $\omega_t = 2\pi \times 1$ MHz. The horizontal grey line indicates the median electric field noise spectral density for all room temperature data points across different size ranges. The black horizontal line is cryogenic data points' median electric field noise. Red points indicate the values measured for two cryogenic setups (PIEDMONS [14] and Dragonfly [15]) in the TIQI group.

Fluctuating electromagnetic radiation could also couple to the experimental setup through wires causing voltage fluctuations on the electrodes. We refer to this as **electromagnetic pickup**. Suppose a conductive loop, A_L , is present in the system, magnetic-field noise B at frequency ω perpendicular to that loop induces a voltage V_L through [18]

$$V_L = \omega B A_L . \quad (2.6)$$

In the presence of a large impedance, this causes a significant voltage drop. Voltage fluctuations can be translated to field fluctuations at the ion's position through the ideal quadruple potential [18],

$$S_E = S_V / D^2 , \quad (2.7)$$

where D is the characteristic distance and can be approximated by the ion-electrode distance d , on which the voltage noise is considered. Similarly, S_E can be obtained through a simulation of the trap potential, where the moment⁴ of the noisy electrode κ is given such that

$$S_E = S_V \kappa^2 . \quad (2.8)$$

Simple approximations lead to values of around $S_E^{(PU)} \sim 10^{-12} \text{ V}^2/\text{m}^2\text{Hz}$ in literature [18], which is comparable to measured level in ion-trap experiments, Figure 1. This is also especially important for cryogenic systems as many connections and large wires ($\gtrsim 50 \text{ cm}$) make them more susceptible to pick-up noise.

Noise can originate in the experimental components themselves. **Johnson-Nyquist noise** is the thermal noise generated by moving charges in conductors. The spectral density of this noise is given through the effective resistance of the circuit in consideration, i.e., [23]

$$S_V^{(JN)} = 4k_B T R(\omega, T) . \quad (2.9)$$

The noise from the trap electrodes is usually negligible due to their relatively low resistance. However, the voltage lines pass through many filter stages for which this noise can quickly become critical. Literature values would approximate $S_E^{(JN)}$ to be on the order $\sim 10^{-13} \text{ V}^2/\text{m}^2\text{Hz}$ [18]. Through electrical models of the circuits in use, an exact calculation of this noise can be obtained.

Finally, **technical noise** should also be considered. Examples of technical noise sources are noisy power supplies or any electrical equipment added to the system by incorrect wiring and could heat the ion through the propagation of the noise through the wires to the electrodes. For typical power supply noise, $1 \mu\text{V}/\text{Hz}^{1/2}$, literature predicts spectral noise densities of $S_E^{(TN)} \sim 10^{-14} \text{ V}^2/\text{m}^2\text{Hz}$ [18].

⁴The moment of an electrode is the linear coefficient of the electric potential created by 1V on that electrode and 0V on all other electrodes.

Noise sources	S_E (V^2/m^2Hz)
Black Body Radiation	10^{-22}
Electromagnetic Pickup	10^{-12}
Johnson Nyquist Noise	10^{-13}
Technical Noise	10^{-14}

Table 2.1: External noise sources and their predicted spectral noise densities S_E based on typical values in ion-trap systems. See [18] for more details.

2.2 Measurement Techniques

Now that we have introduced heating rates and possible noise sources within ion-trap systems, we will list several techniques for measuring heating rates. This will allow us to measure heating rates once we understand what dominates the heating rates of our system and can make changes based on this understanding.

Different methods to measure heating rates exist depending on the system's parameters, as the system (*i*) may or may not be in the resolved sideband regime, which requires the ion's motional frequency ω_t to be larger than the relaxation frequency of the internal states of the ion. The system (*ii*) may or may not be able to be cooled as low as or near the ground state, and (*iii*) we may have heating rates near one quanta/s or near 10^4 quanta/s. The method to use must consider those factors to best extract the heating rates of the system.

2.2.1 Sideband Spectroscopy

To precisely measure heating rates up to 100 quanta/s and for motional states with $\bar{n} \leq 2$, sideband spectroscopy can be used [18]. Sideband spectroscopy uses first-order sideband transitions which can be resolved within the Lamb-Dicke regime, $\eta^2(2n+1) \ll 1$, the regime where the extent of the ion's wave packet is confined to a region much smaller than the wavelength of the transition being addressed [18]. The main processes within this regime along with the carrier transition $|g\rangle \leftrightarrow |e\rangle$, are first-order phonon-assisted red and blue sideband transitions which couple $|g\rangle |n\rangle \leftrightarrow |e\rangle |n \pm 1\rangle$, illustrated in Figure 2.

The Rabi frequencies of the red and blue sideband transitions depend on the motional state of the ion and are given by

$$\begin{aligned}\Omega_{n,n-1} &= \eta\sqrt{n}\Omega \\ \Omega_{n,n+1} &= \eta\sqrt{n+1}\Omega\end{aligned}\tag{2.10}$$

where Ω is the carrier Rabi frequency. The probability of exciting the internal

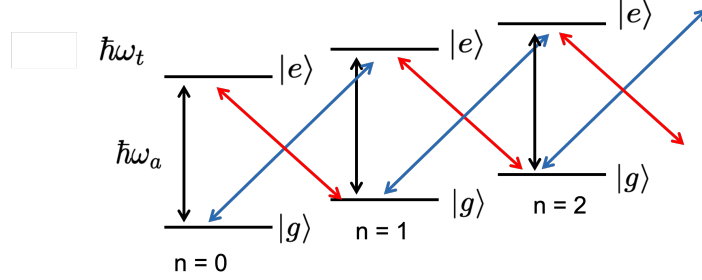


Figure 2: Carrier (black) and motional sideband transitions of the ion. The red sideband couples $|g\rangle |n\rangle$ with $|e\rangle |n-1\rangle$ as shown in red, whereas the blue sideband couples $|g\rangle |n\rangle$ with $|e\rangle |n+1\rangle$.

state of the ion after driving a red or blue sideband for a time t is found to be

$$\begin{aligned}
 p_{|e\rangle}^{RSB}(t) &= \frac{1}{2} \left(1 - \sum_{n=0}^{\infty} P_n \cos(\Omega_{n,n-1} t) \right) \\
 p_{|e\rangle}^{BSB}(t) &= \frac{1}{2} \left(1 - \sum_{n=0}^{\infty} P_n \cos(\Omega_{n,n+1} t) \right)
 \end{aligned}
 \tag{2.11}$$

with P_n the motional state population $|n\rangle$ at $t = 0$. Through the relation (2.10), a Fourier transform of $p_{|e\rangle}(t)$ or a model fit, would allow the extraction of the motional occupancy. By repeating this measurement for different waiting times after cooling, the heating rate $\dot{\bar{n}}$ can be found.

If we assume a thermal distribution of the motional state with an average motional occupancy of \bar{n} , the ratio of red to blue sideband excitation probability can be expressed as [7]

$$\frac{p_{|e\rangle}^{RSB}}{p_{|e\rangle}^{BSB}} = \frac{\bar{n}}{\bar{n} + 1}.
 \tag{2.12}$$

This allows the motional occupancy to be deduced through the asymmetry of the sidebands as illustrated in Figure 3. Repeating the measurement of \bar{n} for different wait times t results in the heating rate $\dot{\bar{n}}$.

2.2.2 Carrier Slowdown Method

For higher motional occupancies within the resolved sideband regime, the carrier slowdown method can be used. With higher phonon numbers \bar{n} , such as the ones achieved without the aid of sub-Doppler cooling, the strength of the carrier Rabi frequency is reduced as higher-order sideband contributions become relevant. The

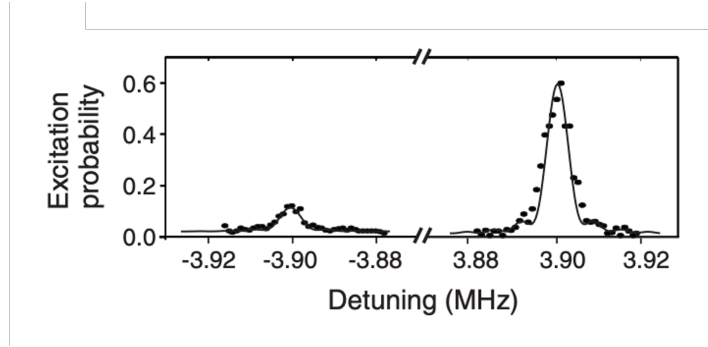


Figure 3: Internal state excitation probability of the ion with a red (left peak) and a blue (right peak) sideband. The relative heights of the peaks could be used to infer the mean phonon number \bar{n} . Taken from [18]

ratio of the reduced carrier Rabi frequency to the close-to-ground state carrier Rabi frequency is given by [24]

$$\frac{\Omega_{\bar{n}}}{\Omega} = \sum_{n=0}^{\infty} P_n \langle n | e^{i\eta(\hat{a} + \hat{a}^\dagger)} | n \rangle = e^{-\eta^2(\bar{n} + 1/2)}, \quad (2.13)$$

wherein the last equality assumes a thermal state. The heating rate can be inferred by repeating the measurement for different wait times t between cooling.

2.2.3 Doppler Recooling

If sideband transitions cannot be resolved, Doppler recoiling can be used to infer the heating rates [25, 26]. This method does not require ground-state cooling and can measure heating rates up to 10^4 quanta/s [18]. Starting with an initially cooled down ion, after a time t , the ion is allowed to heat up, Doppler cooling is re-applied, and the fluorescence of the ion is recorded. As the ion cools down, more and more photons are scattered. This gives the mean phonon number before recoiling. By repeating the measurement for different waiting times t , the heating rates can be calculated. Although this method does not require ground state cooling or sideband resolved transitions, for low heating rates, much longer waiting times are required; in addition, the characterization of heating rates for individual motional modes is difficult.

Ion Trap Setups

In this chapter, we describe the trap geometries and cryogenic setups in which two types of traps, PIEDMONS [14] and Dragonfly [15], have been experimentally measured. Differences in the trap symmetries will be referred to in later chapters for noise calculations. Moreover, modifications to the setups are taken relative to the configurations detailed in this chapter.

3.1 Traps

3.1.1 Dragonfly Trap

The Dragonfly is a 3D symmetric trap made of a stack of five silica glass wafers [24]. Two wafers host the control (DC/RF) electrodes with a spacer wafer in the center. The leftover wafers host the shim electrodes, as shown in Figure 4 (a).

The trap hosts 106 DC control electrodes, one RF electrode, and 36 DC shim electrodes for compensating stray electric fields. The separation of the electrodes in the xz plane is $300\ \mu\text{m}$ and $220\ \mu\text{m}$ in the y direction, accounting for an ion-electrode separation of $185\ \mu\text{m}$. The trap axis is chosen as the z -axis. Figure 4 (b) shows a top view of the control wafers. The trap hosts several zones, including loading and experimental zones. Further details on the zones, structure, and electrode dimensions can be found in [24].

3.1.2 PIEDMONS Trap

Moving on to a slightly less symmetric yet 3D trap, we introduce the PIEDMONS trap [14], shown in Figure 5.

The PIEDMONS trap is a hybrid 3D trap consisting of a surface trap with a top layer hosting two DC electrodes. This can enhance the potential's depth compared to simple surface traps. The ion is held at a distance of $200\ \mu\text{m}$ from the closest electrode. A glass wafer separates the top and bottom wafer with a thickness of $400\ \mu\text{m}$. The slit in the top-wafer electrodes provides optical

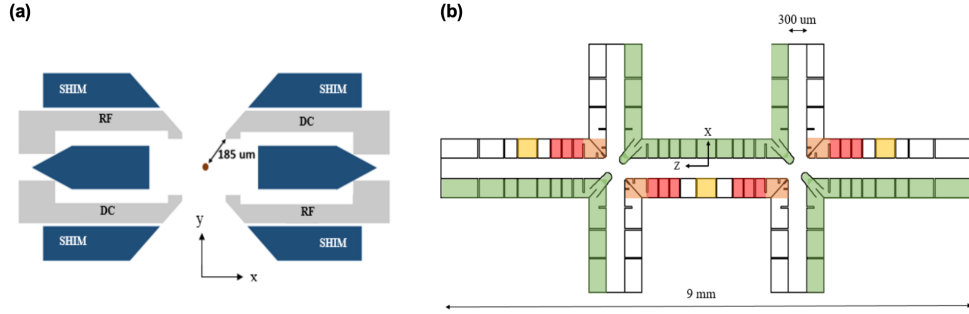


Figure 4: Dragonfly trap design [15,24] (a) Side view of the five stack wafers. The control electrode-carrying wafers are interposed between the outer shim stacks and the inner spacer stacks. (b) Top view of one of the control electrodes-carrying wafers. The RF electrodes are shaded green. The DC electrodes shaded in yellow are trapping zones, whereas the red-shaded electrodes are for merging and splitting potentials. The orange-shaded electrodes are for the transport of the ions. The second control electrode-carrying wafer is inverted with the RF electrodes reversed across the axis, creating a 3D trap.

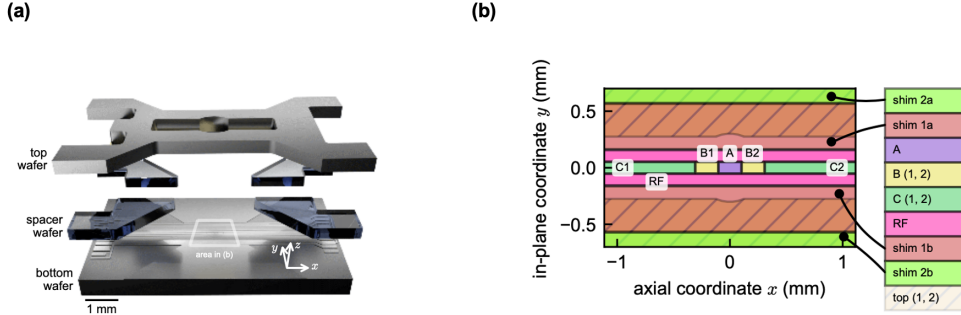


Figure 5: PIEDMONS trap [14] (a) View of the three wafers. The top wafer hosts two DC electrodes. Spacer wafers are sandwiched between the top wafer and the bottom wafer, which holds a surface trap with nine DC electrodes and one RF electrode. (b) Top schematic of all 12 electrodes. Cross-hatched pattern indicates the top electrodes.

access for fluorescence detection. Further details on the dimensions and trap characteristics can be found in [14].

A top view of the trap electrodes can be seen in Figure 5 (b). The bottom wafer contains nine DC electrodes and one RF electrodes. The central electrodes (A, B1, B2, C1, C2) provide axial confinement (x -axis) at several positions, whereas the remaining electrodes are used for stray field compensation. The top electrodes are indicated by a cross-hatched pattern.

Extensive heating rate measurements for different parameters and setup changes were performed on the PIEDMONS trap and will therefore be the main focus of this thesis. Comparison with observed heating rates of the Dragonfly trap will help understand and draw conclusions on the noise sources.

3.2 Surrounding Environment

Though the traps mentioned above differ in geometry, their setups are very similar in design and equipment. For instance, the setups use the same cryogenic cooling apparatus and are subject to similar levels of external field noise. The following section summarizes essential parts of the setups required for heating rate considerations.

3.2.1 Cryogenic System

Both traps are placed within the inner chamber of a closed-cycle cryostat, reaching temperatures around $\sim 4 - 6$ K. A heat shield at 40 K surrounds the inner chamber, which is surrounded by a room-temperature vacuum chamber. Figure 6 shows the layers of the cryostat. The inner chamber includes superconducting coils (for stable currents and external field cancellation), a helical resonator (RF lines), and a trap carrier PCB. External coils mounted on the vacuum chamber viewports can produce a field that can be locked into the superconducting coils when they are superconducting, thus allowing the spectral separation of Zeeman sublevels. Effusive ovens are mounted on the vacuum chamber viewports, producing neutral calcium beams when current is applied.

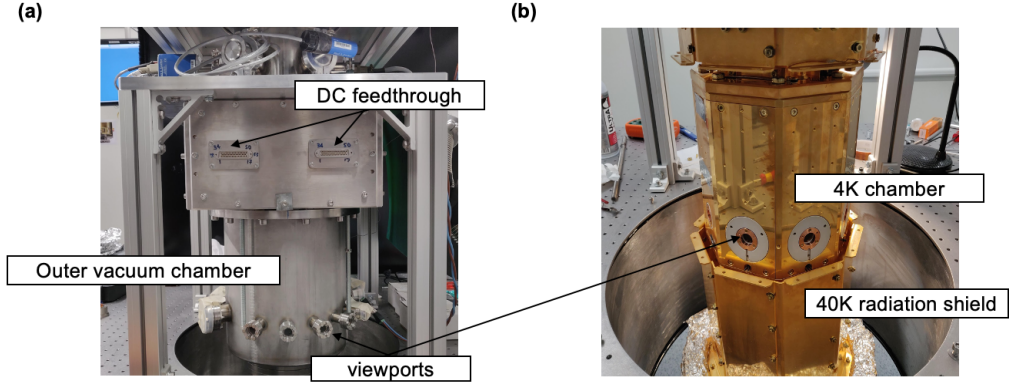


Figure 6: Images of the cryogenic apparatus (a) The outer vacuum chamber with viewports for beam access can be seen. DC feedthrough connections for mounting outside DC electronics. (b) Inner shells of the cryostat. The 40 K radiation shield unscrewed and lowered, displaying the innermost 4 K chamber. Adapted from [24].

The ion trapped in both setups is calcium $^{40}\text{Ca}^+$. Lasers perform manipulation, state preparation, and readout of the internal states. The optical system with the relevant lasers (Calcium: 397, 866, 854, 423, 729 nm) for photo-ionization, state initialization, cooling, state manipulation, and detection of the ion can be seen in Figure 7.

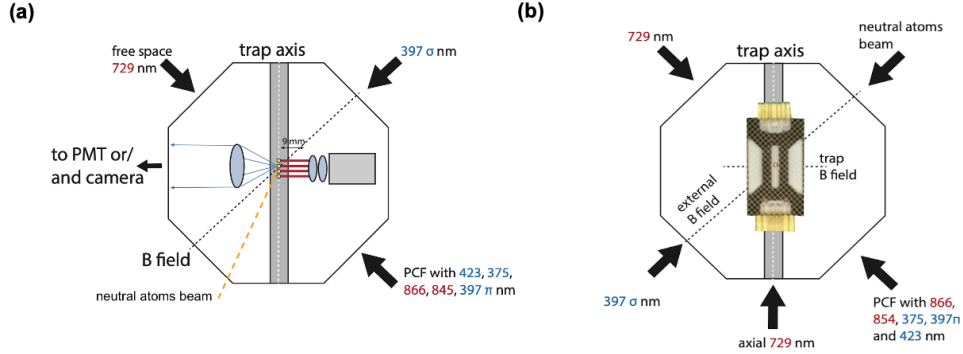


Figure 7: Beam orientation and magnetic field direction for (a) Dragonfly and the (b) PIEDMONS setup. Imaging of the PIEDMONS setup attached to the bottom of the vacuum chamber.

The imaging objective in the PIEDMONS setup is attached to the bottom of the vacuum chamber rather than in the inner chamber, as in the Dragonfly setup. This extends the compatibility of the setup for planar traps, where the trap surface typically points downwards, and beams come across the trap surface. More on the optical and cryogenic system of both setups can be found in Chiara

Decalori [24] or Robin Oswald's PhD thesis.

3.2.2 Voltage Lines

The DC and RF electrical lines are supplied to the traps through a final filtering stage, at the base of the cryostat, to which the traps are directly mounted. The complete path for delivering DC voltages will be described below.

DC lines

The DC voltages in the PIEDMONS trap are generated by a DAC¹ (Digital-to-Analog Converter) up to ± 10 V, followed by low-noise operational amplifiers² with a gain of about 2.8. A filtering stage follows to suppress electric noise up to this point. Flexible cables³ (≈ 76 cm) carry the signal lines from the first filtering stage at 300 K to the last cryogenic filtering stage at 4 K. The trap is glued and wirebonded to this cryogenic filter board. The electronic model for the outside and cryogenic filters can be seen in Figure 8 (a).

The DC lines in the Dragonfly setup differ slightly. For instance, voltages for the control electrodes are created by DEATHs (Direct Ethernet Adjustable Transport Hardware [27]). These have the advantage of a fast switching rate of the generated voltages, intended for coherent transport of ions. While the shim electrodes, which are used for stray field compensation, are supplied by a DAC⁴. Figure 8 (b) shows the outer filtering stage and cryogenic filters. Homemade Kapton-insulated manganin wires (≈ 60 cm) carry the DC lines to the cryogenic filterboard. The trap is suspended on a hole inside the cryogenic filter board. The DC and RF are electrically connected to the filterboard through wirebonds. The low-pass RC cryogenic filters in the Dragonfly and PIEDMONS setup differ significantly in the cut-off frequency with 809 kHz and 40 kHz, respectively. The cryogenic filters in the PIEDMONS trap have better filtering at higher frequencies. Our interest lies in the frequency range around the ion's motional trap frequency, which can be adjusted through the RF amplitude and DC potential to a range typically within (0.5 - 5) MHz. The filtering can be quantified by comparing the voltage gain curves of both setups, Figure 9. The gain curve is defined as the modulus of the transfer function, which relates the system's output voltage to its input voltage:

$$|H(\omega)| = \left| \frac{V_{Out}}{V_{in}} \right|. \quad (3.1)$$

¹AD5731

²ADA4522-2

³FFC Molex 150151051

⁴AD5370

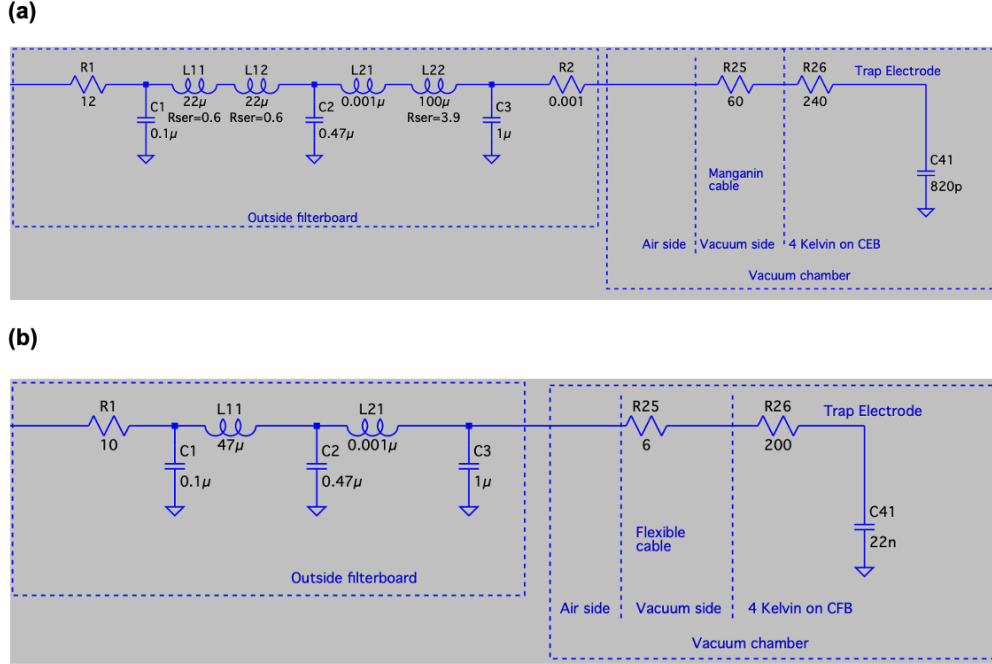


Figure 8: LTSpice model of the filtering stages for (a) Dragonfly and (b) PIEDMONS setup. The outside and cryogenic filterboards are indicated by dashed rectangles. While outside filterboards are similar, cryogenic filterboard cut-off frequencies are at 809 kHz and 40 kHz for (a) and (b), respectively.

The gain curve of the PIEDMONS filters, Figure 9 (a), is about an order of magnitude lower; hence if the same amount of noise power enters both filters, the noise at the output of the Dragonfly setup is expected to be 100 times larger.

RF lines

The RF signals for the PIEDMONS and Dragonfly trap are provided by a signal generator⁵, followed by an external amplifier⁶. Voltages are delivered to the inner chamber through stainless steel⁷ coaxial cables. A helical coil resonator [28] is used, allowing for low-noise voltage amplification at the resonator frequency and impedance matching of the trap RF electrodes to the rest of the circuit. This improves power transmission efficiency and reduces power requirement of the source. The resonator can be seen in Figure 10; it consists of a coil for which one end is connected to an outer shield, while the other end is connected to the RF electrode. A small antenna coil is placed within the larger coil and couples

⁵Rohde & Schwarz. SMC100A

⁶Mini-Circuits ZHL-1-2WX-S+

⁷Coax Co., Ltd. SC-086/50-SS-SS

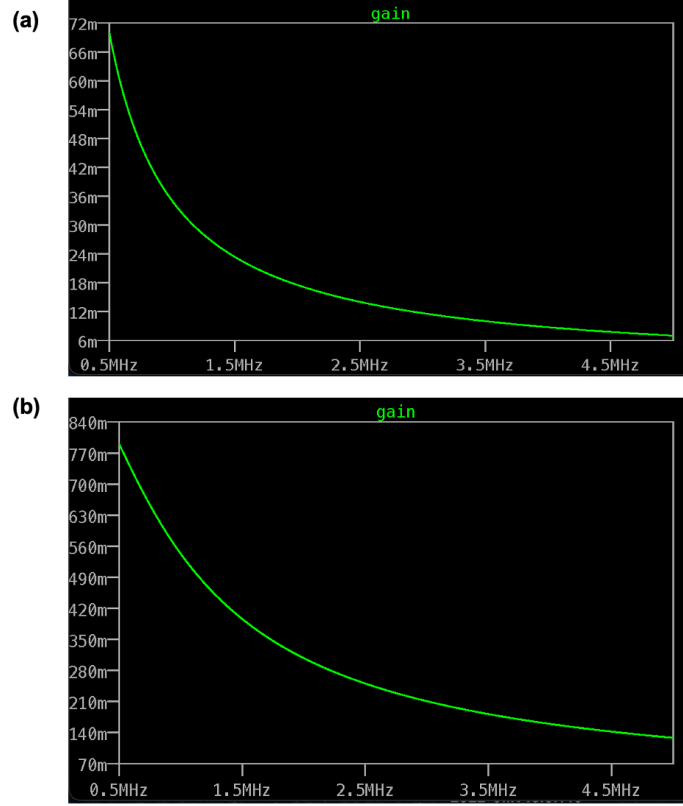


Figure 9: The gain curve of the cryogenic filterboards for a relevant frequency range. The PIEDMONS filters (a) show a lower gain curve than the cryogenic filters for the Dragonfly trap (b).

the signal inductively to the resonator. Impedance matching is achieved by mechanically tuning the position of the coupling coil relative to the main helical coil. However, the impedance matching in a cryogenic temperature is different from that at room temperature. This effect must be taken into consideration and compensated to achieve matching at the operating temperature. The resonance peak for the PIEDMONS circuit is observed at 20.6 MHz and thus chosen as the RF drive frequency, while the Dragonfly drive frequency is at 36.3 MHz. Respective quality factors of $Q \approx 165$ and $Q \approx 140$ are measured. These allows signals up to 200-300 V. The RF circuit includes other components such as a capacitive pick-off and rectifier for connectivity and monitoring signals. The electronic model includes all these components.

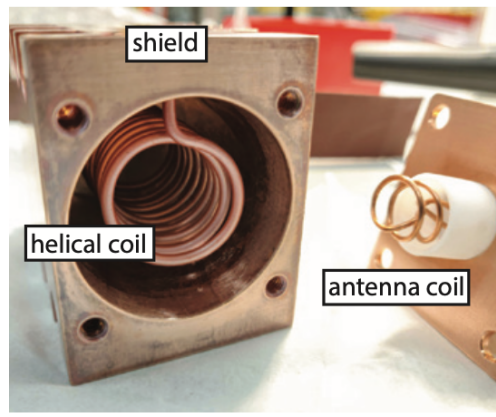


Figure 10: Helical resonator used for RF voltage supply amplification. The helical coil couples inductively to the antenna coil so that impedance matching with the trap can be achieved.

3.2.3 Grounding

We briefly review the setups' grounding configuration, which will be significant for later chapters.

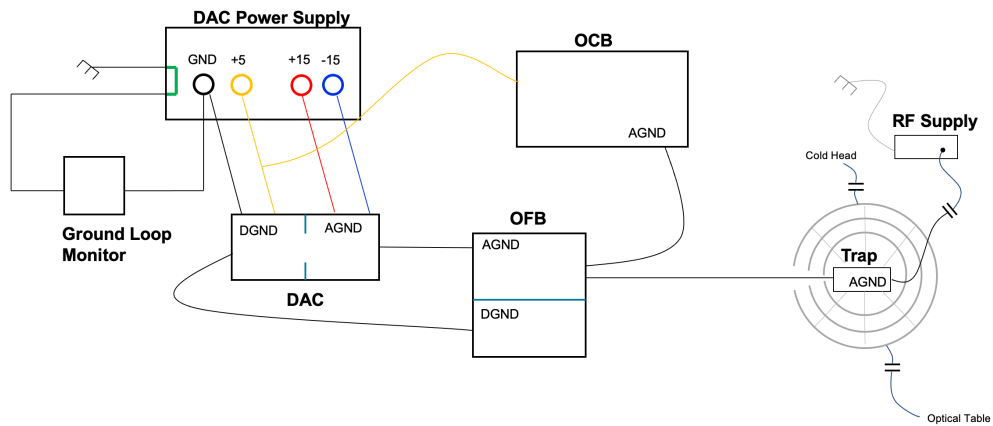


Figure 11: Grounding configuration for the PIEDMONS setup. Ground referenced to the DAC, which is earthed through the DAC power supply case indicated in green.

The ground reference is chosen to be the DAC ground which is earthed through the DAC power supply case to the mains ground of the building, indicated in green in Figure 11. A ground loop monitor checks for any ground loops within the external components and supplies connected to the mains ground. The DAC and outer filters sit on an outer connectorboard mounted at the feedthrough

of the cryostat, Figure 6. FFC cables connect the outer filter ground to the trap ground. The RF Signal Lines are DC blocked before entering the cryostat. This is to prevent DC frequencies to interfere with the RF components.

We opt for a chassis configuration in the system, i.e., we reference ground lines of different parts to multiple points such that they meet everywhere frequently. This can effectively prevent large ground loops in the system, reducing pickup noise. This configuration is implemented as follows: the trap ground plane is connected to the cryostat's 4 K chamber, which is electrically connected to the two outer shells of the cryostat. The ground at the outer filter board is connected to the cryostat through a thin jumper wire. This offers a relatively low impedance path to the ground compared to the return currents through the lengthy FFC wires. This connection means that the return current from the trap goes through the metal conductor (cryostat). For the PIEDMONS and the Dragonfly trap, heating rates with the chassis grounding were three orders of magnitude lower than those measured with the conventional grounding lines. We refer to this observation again in the later chapters; however, calculations and measurements in this thesis will consider a chassis configuration unless stated otherwise. Though it is difficult to measure the system's resistance in this configuration, we estimate that it is very small ($\ll 1$) and hence make an approximation of a zero resistance path of the electrodes to ground in the electronic circuit models, Figure 8.

Technical Concepts and Appropriate Devices

In Chapter 2, we have mentioned technical noise as a source of ion heating. To investigate how technical noise in different parts of the system could lead to noise at the ion, it is essential to know the procedure for measuring noise. In the following, we will introduce basic concepts of noise measurements and draw comparisons of measurement devices present in our lab.

4.1 Noise Spectral Density

We have seen previously that electrical noise on the electrodes results in electric field noise on the ion. The quantity we use to characterize voltage noise is the power noise spectral density (PSD), given in units of V^2/Hz . Manufacturers tend to express noise through the amplitude noise spectral density, $V/\sqrt{\text{Hz}}$, the square root of the PSD. This is defined as the average power of the noise at different frequencies within a bandwidth of interest.

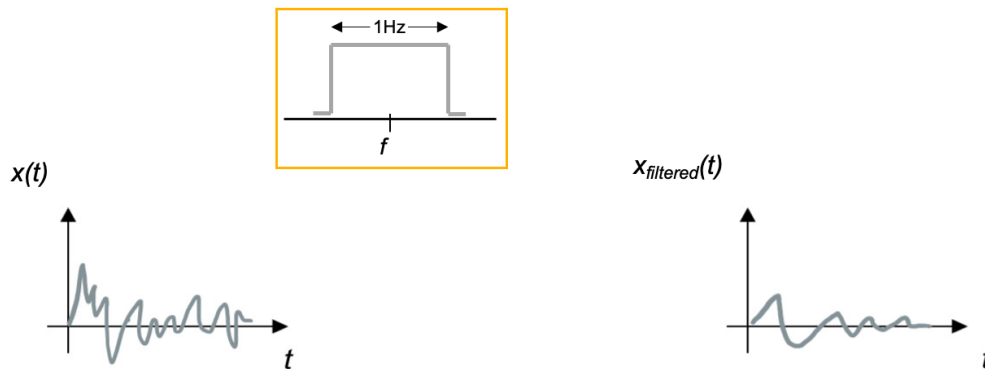


Figure 12: Schematic illustrating how noise spectral density is computed. Power spectral density at f of $x(t)$ is the estimated power of the filtered signal $x_{\text{filtered}}(t)$

To properly visualize this quantity, suppose we are given a noise signal $x(t)$. To find the average noise power at a frequency f , we could apply an ideal band-

pass filter with a bandwidth of 1 Hz centered around f . The average noise power measured after the bandpass filter estimates the average power of the noise at frequency f . By repeating this procedure for all frequencies within a bandwidth of interest, the noise spectral density vs. frequency can be obtained.

4.1.1 Resolution- vs Noise Equivalent- Bandwidth

In practice, bandpass filters have a roll-off region into the stopband rather than an abrupt transition. Therefore, noise components in the roll-off region are only partially suppressed and one would have to account for the noise power within those frequencies. We define therefore the noise-equivalent bandwidth as the bandwidth of a fictitious rectangular filter with the same amount of noise power as that of the actual filter, Figure 13.

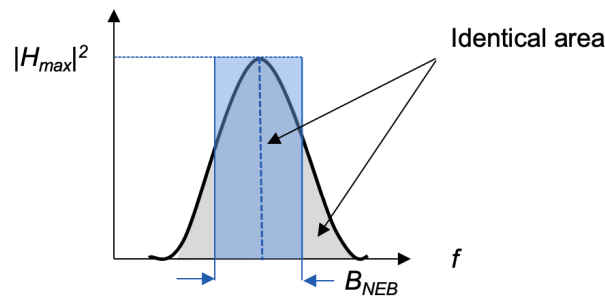


Figure 13: Filter transfer function $H(f)$ and noise equivalent bandwidth B_{NEB} of ideal filter with identical area.

If the filter at hand has a transfer function $H(f)$, the noise-equivalent bandwidth is given by

$$B_{NEB} = \int_0^{\infty} \left| \frac{H(f)}{H_{max}} \right|^2 d\omega, \quad (4.1)$$

where H_{max} is the maximum value of $|H(f)|$.

This becomes important when measuring noise, as some devices only measure the power signal and cannot measure in V^2/Hz . If the filter used within the measurement device is not known, we use the resolution bandwidth (RBW) as a first approximation. This is the bandwidth of the final filter applied to the input signal in the device. The conversion from power, in dBm, to noise spectral density is then given by

$$\text{PSD [V}^2/\text{Hz]} \approx \frac{R_{term} * 0.001 * 10^{P_{dBm}/10}}{\text{RBW}}, \quad (4.2)$$

where R_{term} is the termination resistance of the measurement device (typically 50Ω).

For first-order low-pass filters, the noise-equivalent bandwidth to resolution bandwidth ratio would be 1.57. As the order of the filter increases, this factor would converge to 1. However, this argument is not valid when distinct cascaded filters are present within the device.

4.2 Noise Propagation

This section will review the concept of noise propagation as it is extensively used within the thesis. For instance, if the noise is measured at a specific point in the circuit, noise propagation allows the prediction of the noise at a later stage in the circuit. Consider this simple low-pass RC filter in Figure 14.

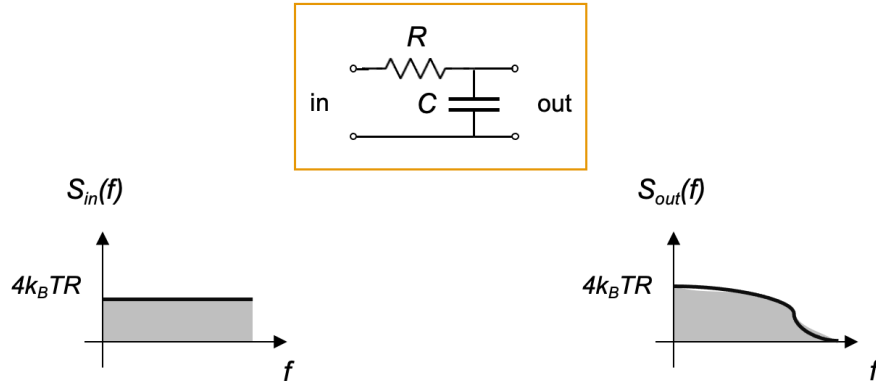


Figure 14: Noise spectral density of low-pass filter RC at the output node.

The noise generated in this circuit is the thermal noise of the resistor R , given by $S_{V,in} = 4k_B T R$. This noise propagates to the output of this circuit through the relation

$$S_{V,out}(f) = S_{V,in}(f) |H(f)|^2, \quad (4.3)$$

where $|H(f)|$ is the gain of the circuit. For larger systems, separation into sub-circuits for which the noise and transfer function can be calculated is recommended. The noise can then be propagated to a certain position along the lines through the transfer function of the sub-circuit blocks.

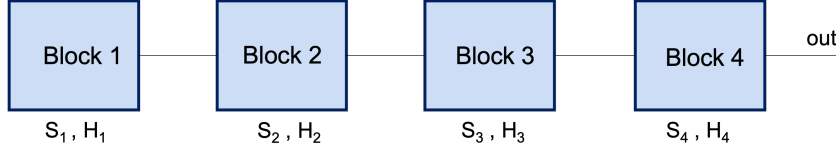


Figure 15: Circuit fragmented into sub-circuits with input-referred noise spectral density S_1 and transfer function H_1 .

For instance, the total noise at the output node (out) in Figure 4.4 is given by

$$\begin{aligned}
 S_{V,out}(f) &= S_{V_1,in}(f)|H_1(f)H_2(f)H_3(f)H_4(f)|^2 \\
 &+ S_{V_2,in}|H_2(f)H_3(f)H_4(f)|^2 \\
 &+ S_{V_3,in}(f)|H_3(f)H_4(f)|^2 \\
 &+ S_{V_4,in}(f)|H_4(f)|^2 .
 \end{aligned} \tag{4.4}$$

If the output noise of each sub-circuit is known this can be reduced to

$$\begin{aligned}
 S_{V,out}(f) &= S_{V_1,out}(f)|H_2(f)H_3(f)H_4(f)|^2 \\
 &+ S_{V_2,out}|H_3(f)H_4(f)|^2 \\
 &+ S_{V_3,out}(f)|H_4(f)|^2 \\
 &+ S_{V_4,out}(f) .
 \end{aligned} \tag{4.5}$$

4.3 Device Comparison for Noise Measurements

Spectrum analyzers are great devices to use for measuring signals, including noise. However, the correct settings must be chosen for noise measurements to offer the best results. Spectrum analyzers sample more data points that can be possibly displayed; hence a certain way to summarize the data in each pixel should be chosen. The correct detector type for noise measurements would be the RMS average detector, which averages the data points allocated to each pixel and presents the average on the displayed pixel on the screen. Moreover, trace modes that can be selected independently of detector types exist. We set the trace mode to normal (clear/write), i.e., the instantaneous trace of the signal.

In the following, we will compare three devices at our disposal regarding noise floor and operation at the desired frequency regime, (0.5 – 5) MHz.

We start by looking at the **Analog Discovery Kit 2**, ADK, as it can display the noise spectral density in V^2/Hz up to 2 MHz. The Analog Discovery Kit

is a powerful tool as it can be used not only as a spectrum analyzer but also as an impedance analyzer, oscilloscope, and more. However, this device has a noise floor of $\sim 400 \text{ nV}/\sqrt{\text{Hz}}$, which is higher than the level of noise we are interested in, $\sim 100 \text{ nV}/\sqrt{\text{Hz}}$. The noise floor dilemma could be overcome by adding a preamplifier before the measurement device. A preamplifier was used on a noise source with the ADK. The noise spectral density can be seen in Figure 16. Surprisingly, a forest of giant resonances overshadows the general noise trend of the source, ruining the measurement. Some of those peaks were observed with the ADK device alone. The origin of those peaks is not understood, although some have been observed on the device itself without amplification. An interplay between the amplifier and the ADK could result in the resonances that were not present on the amplifier or ADK alone. Furthermore, the signal post-processing of the ADK may also be the culprit. This would need to be investigated further.

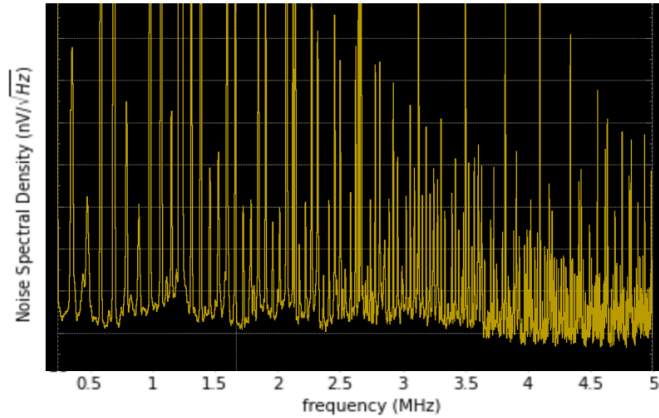


Figure 16: Noise measurement of an amplified noisy source with ADK. Large resonances dominate the spectrum overshadowing the source's noise.

Noise signals can just as well be measured with oscilloscopes. By choosing an appropriate sample rate, a fast Fourier transform of the noise signal can be performed to obtain the noise spectral density. The noise floor of the oscilloscope at our disposal, **Rigol MSO5074**, was measured to be $\sim 80 \text{ nV}/\sqrt{\text{Hz}}$.

The last device on our list is the **RF Analyzer N9912A**, which will refer to as the Fieldfox. It is extensively used in our lab due to its ability to measure frequencies up to 4 GHz. Its noise floor is comparably low $\sim 40 \text{ nV}/\sqrt{\text{Hz}}$. The Fieldfox can only measure the noise power in dBm; hence Equation (4.2) is used to obtain the noise spectral density.

As with the ADK, we use a preamplifier to measure a noise source with the Fieldfox and oscilloscope for characterization. The noise measurements are shown in Figure 17.

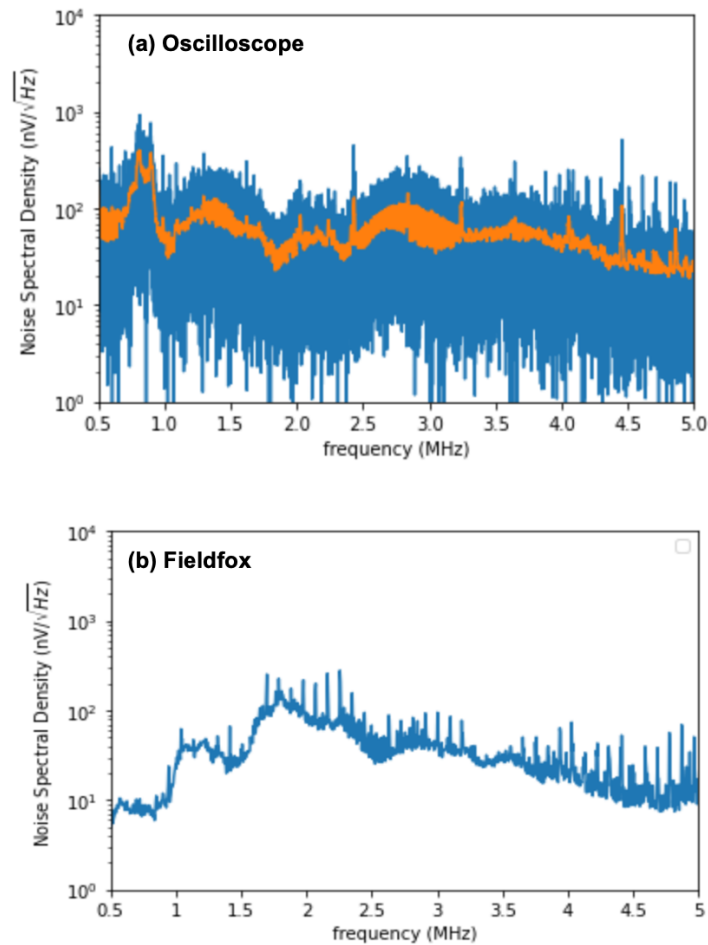


Figure 17: Noise measurement of an amplified noisy source with (a) Oscilloscope and (b) Fieldfox. The orange trace in (b) displays the moving average of the measured data in blue. Above 2 MHz, spectra follow the same trend and exhibit the same noise level. Towards DC, the source’s noise measured with the Fieldfox rolls off.

We confirm our approximation to be reasonable since the noise levels for both devices are very similar (orange trace). Although a clear roll off of the noise amplitude below 2 MHz is visible from Fieldfox measurement. The Fieldfox can identify noise below this frequency; however, the amplitude of this noise is not reliable. The datasheet mentions specifications for frequencies starting at 2 MHz, suggesting it as the lower limit of this device. Various other devices exist, such as the **SR760 Stanford Research Spectrum Analyzer** with a relatively low noise floor of $7 \text{ nV}/\sqrt{\text{Hz}}$; however, these either operate up to 100 kHz or starting 10 MHz frequencies. Consequently, the oscilloscope and the preamplifier seem

to be the most reliable tools for measuring noise below $100 \text{ nV}/\sqrt{\text{Hz}}$ and at a frequency range of $(0.5 - 5) \text{ MHz}$.

All measurements in the upcoming chapter have been taken before this characterization and making of the preamplifier board. Therefore, the measurement device used was the Fieldfox with its lower noise floor.

Modeling External Noise Sources: PIEDMONS Trap

This chapter will address the observed heating rates of the PIEDMONS trap. Various models of possible heating mechanisms will be compared to the observations to pinpoint the most probable noise source. Moreover, the Dragonfly trap heating rates will be discussed to establish trends between the setups.

5.1 Measured Heating Rates

In Chapter 3, we discussed the details of the PIEDMONS setup. Prior to this work, heating rate measurements for characterization of the PIEDMONS trap have been done on a single trapped $^{40}\text{Ca}^+$ ion as described in [14]. Through micromotion compensation, the stray electric fields pushing the ion away from the RF null are inferred and consequently compensated for through voltages on the shim electrodes. Using the sideband ratio method (see Chapter 2.2), the axial (x -axis), and radial heating rates were measured. The radial modes do not necessarily align with the Cartesian coordinates and can be rotated with respect to the trap's surface. Thus, we denote the in-plane and out-of-plane modes by y' -axis and z' -axis, respectively. The measured heating rates vs three different system parameters are shown in Figure 18.

In Figure 18 (a)-(b)¹, the heating rates are plotted as a function of frequency f and trap temperature T_{trap} . The radial modes are rotated by 38° from the xy -plane. This allows both radial modes to be accessed by laser beams for cooling. The axial mode rates follow a power law scaling with trap temperature and frequency, namely $\Gamma \propto \omega^{-\alpha} T_{trap}^\beta$ with $\alpha = 2.3(1)$ and $\beta = 1.34(8)$ extracted from the fits. This is consistent with scaling exponents found from surface noise effects [29]. The radial heating rates, however, exhibit a large scatter relative to the uncertainty of each point [14]. A weak correlation of the trap surface temperature with the radial heating rates suggests noise arising from external sources.

¹ Measured heating rates in 18 (b) and (c) were normalized to frequencies using the frequency dependence in 18 (a), see [14] for further details.

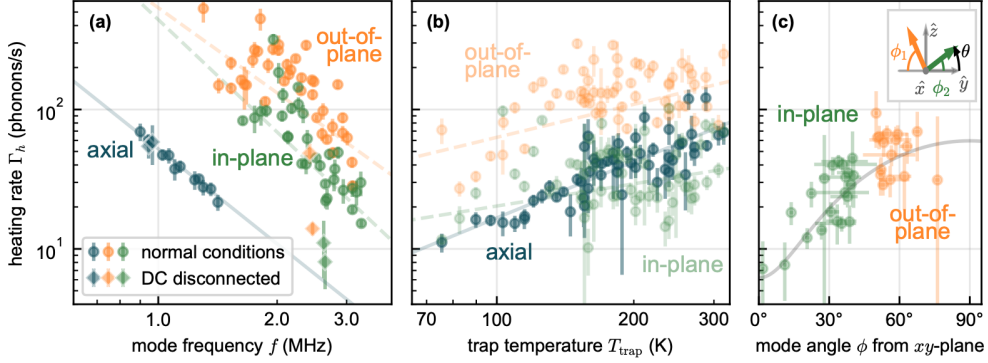


Figure 18: Measured heating rates of axial and radial modes vs frequency f , trap temperature T_{trap} , and mode orientation ϕ from xy -plane. (a) Axial frequencies varied with adjusting DC voltages, whereas radial mode frequencies were varied with adjusting RF power voltage, with a 38° orientation of the modes relative to the xy -plane. Axial heating rates follow a power law scaling with frequency whereas radials exhibit large scatter. Heating rates with DC lines disconnected are plotted with diamond shaped points. (b) Through a nearby heater, the temperature of the trap was varied. The radials show weak correlation with the trap temperature, while the axial increases linearly with the temperature. The measured heating rates were frequency normalized (see text) to (0.98, 2.35, 2.56) for axial, in- and out-of plane modes. (c) Rotation of the modes adjusted through DC voltages such that θ varies from 0° to 45° . The trap temperature was set to be 185 K and the frequencies were normalized (see text) to 3 MHz for the in- and out-of plane modes.

Moreover, the radial heating rates were significantly reduced when DC lines were disconnected, i.e. disconnecting DC voltage sources and ground references. The axial heating rates were not affected by this, pointing further to the fact that axial and radial heating rates are limited by separate noise sources, surface and external noise respectively.

Figure 18 (c) ¹ shows the heating rates based on changing the rotation angle θ from the xy -plane. The heating rates were plotted for theta between 0° and 45° . We can express this angle through the ϕ_1 and ϕ_2 , which describe the in- and out-of-plane mode angle from the xy -plane, respectively. The heating rates show a significant increase with rotation of the modes from in-plane to out-of-plane, pointing towards a certain polarizability of the noise.

5.2 DC Circuit Noise

Following the observations mentioned in the previous section, the DC circuit is the most suitable candidate to investigate. To understand whether noise is generated by Johnson noise in circuit components, or whether external noise is passed through the entire circuit, we produce a model of circuit components that connect each DAC channel to an electrode. Figure 19 (a) shows a schematic of the DC line components. The voltage line components were introduced in Section 3.2.2. The DAC, amplifiers, and the outer filterboard (OFB) sits on an outer connectorboard (OCB) which can be mounted on the outer vacuum chamber feedthrough, Figure 19 (b). FFC cables route the DC lines to the cryogenic filterboard (CFB) on which the trap is mounted.

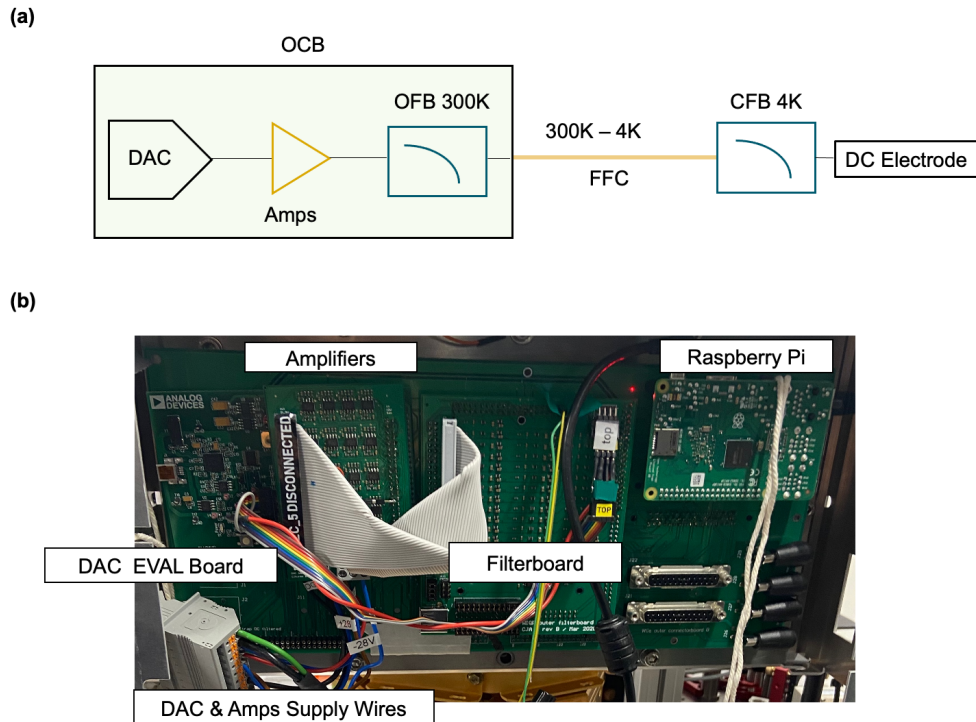


Figure 19: DC voltage circuit lines. (a) Schematic of the DC voltage lines. A DAC supplies voltages up to ± 10 V, which are amplified and filtered through the outer filterboard (OFB). These sit on an outer connectorboard (OCB) which is mounted on the cryostat feedthrough. Voltage lines are carried by FFC cables to a second filtering stage inside the 4K chamber (CFB) onto which the trap is wirebonded. (b) The outer connector PCB with wires for the DAC and Amplifier supplies, DAC -, amplifier- and filter- PCBs. A Raspberry Pi is used to control the DAC.

We can evaluate the Johnson noise at the trap electrode of this circuit for relevant trap frequencies between 0.5 and 5 MHz through an electronic simulation. To include the noise of the DAC at those frequencies², we measure the noise directly at the DAC output. No voltage is applied on the electrode channels since the model we assume does not depend on the source voltage value. The total noise at the trap electrode is given by the sum of the propagated DAC noise and the in-circuit generated noise (Section 4.2). Each electrode is subject to the same noise due to identical circuit lines. Within this Johnson noise model, we assume uncorrelated noise between the electrodes. The power noise spectral density on each electrode is converted into electric-field noise spectral density using a trap simulation, Equation (2.8). We set the tilt the radial modes to be at $\theta = 38^\circ$ from xy -plane. This allows a one-to-one comparison with the measured heating rates in Figure 18 (a). We then sum the electric-field noise spectral density of each of the 11 DC electrodes and use Equation 2.4 to compute the expected heating rates. Figure 20 shows the expected heating rates (lines) vs frequency plot from the DC circuit (lines) compared to the measured heating rates (crosses).

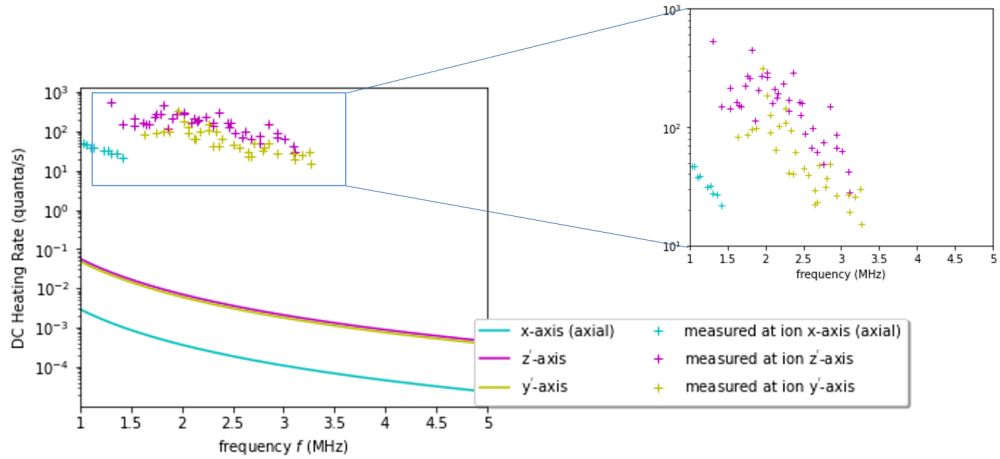


Figure 20: Expected heating rates (lines) from Johnson noise of the DC circuit vs measured heating rates (crosses). The radials are tilted by $\theta = 38^\circ$ from xy -plane. The expected axial- and radial- heating rates are three orders of magnitude lower and follow a smooth curve in contrast to the scatter evident in the measured values on the right.

Figure 20 shows that the expected heating rates follow a smooth curve almost three orders of magnitude lower than the measured heating rates. Moreover, this simple DC circuit model cannot explain the large scatter within the radials.

Previous characterization of the OFB showed an irregular behavior as we go

²The datasheet for the DC source (AD5731) displays the noise up to only 5 Hz

towards the MHz regime. Though we suspect the measurement probes used for this characterization to be loading the circuit, we opt for a second set of noise measurements at the OFB³. The noise spectral density measured with the Fieldfox spectrum analyzer can be seen in Figure 21 (b). The spectrum is noisy, especially around 2–3 MHz, where the radial modes are situated for many configurations. Below 1.5 MHz, the noise of the measurement reaches device noise floor.

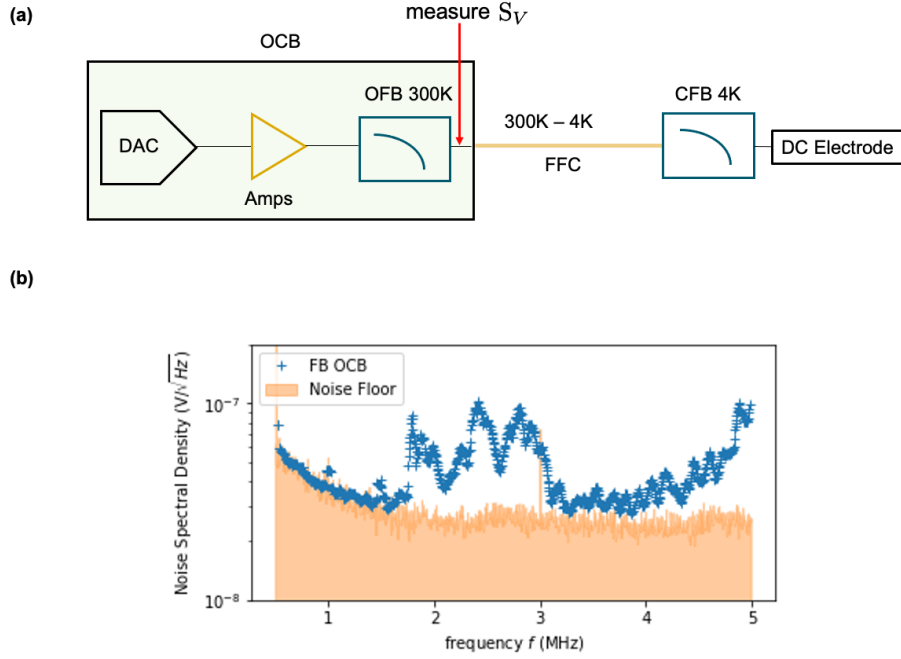


Figure 21: (a) Schematic of power noise spectral density measurement at the OFB of the DC circuit. Measurement result (b) shows large peaks around typical radial frequencies (2–3 MHz). Increasing noise towards 5 MHz is possibly due to measurement probes.

We assume that when the OFB is reconnected to the trap, the same noise will propagate through the last block of the circuit, i.e. the cryogenic filterboard, to the electrodes. With the previous assumption of uncorrelated noise, the expected heating rates can be seen in Figure 22.

The noise measured at the outer filterboard is somewhat suppressed through the cryogenic RC filter; however, it propagates to the electrodes causing the scatter seen in the measured heating rates (red crosses) for the radials. Towards the axial frequencies, we cannot distinguish the noise from the device noise floor

³The OCB must be disconnected at the feedthrough for the measurement. Otherwise, the current flows towards the signal lines in the cryostat rather than to our measurement device.

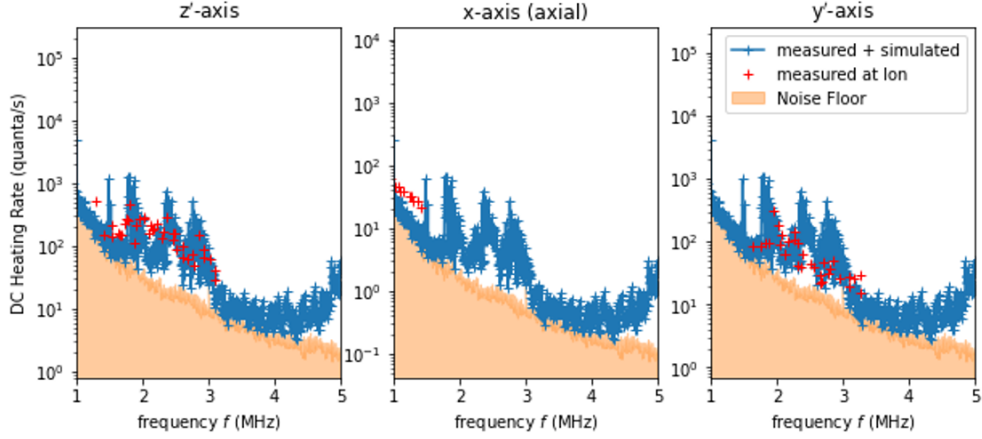


Figure 22: Expected heating rates from outer filterboard measurement (blue traces) vs. measured heating rates at the ion (red crosses). The radials are tilted by $\theta = 38^\circ$ from xy -plane. Scatter matches the measured trend in the radials. Device noise floor dominates towards axial frequencies, nevertheless axial mode mainly limited by surface effects

at the filterboard. The measured axial heating rates are nevertheless higher than expected from the noise floor of the device and are further very likely limited by surface effects. A characterization to identify the noise source will be described in the following.

5.2.1 Source Characterization

To eliminate the noise peaks seen in Figure 22, the source has to be found. The wide size of the peaks in Figure 22 suggests pick-up noise. The OFB includes multiple inductances and jumpers, easily susceptible to pickup. Additional measurements at the OCB showed a similar noise trace with larger amplitudes. This prompted several measurements for the characterization of the noise source. To learn whether the noise originates in the OFB components or the OCB, we compare the noise signal of the OFB at the OCB, Figure 23 (a), to (i) a replica OFB at a different location, Figure 23 (b), and (ii) a simplified, well-shielded RC filter with the same cut-off frequency as the OFB, Figure 23 (c). These measurements produce almost identical traces. We, therefore, conclude that the noise does not start at the OFB nor the OCB and originates at an earlier point.

Placing the measurement probes back to the OFB at the OCB, we turn to the grounding configuration of the setup. For all the previous measurements, the ground reference was chosen to be DAC ground (see green line in Figure 11),

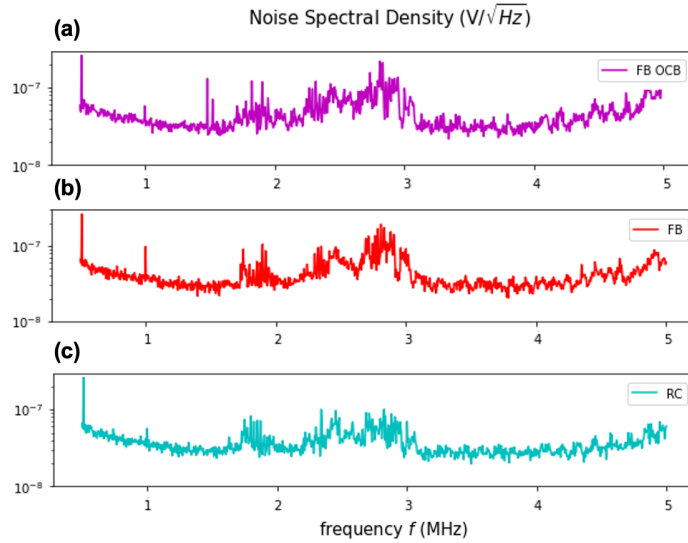


Figure 23: Noise spectral density measurements for different configurations. For all three measurements the DAC was connected. (a) Measured at the OFB on the same OCB as the DAC. (b) Measured at a replica OFB at a different location than the OCB. (c) Measured at a simple RC filter with the same cut-off frequency as OFB. Peaks are present in every configuration, suggesting neither the OCB nor the OFB to be the culprit of the noise.

as described in Section 3.2.3. We now choose to ground the voltage lines to an earthed copper pipe. Furthermore, we disconnect the ground loop monitor due to an inadequate power supply that was observed to add some noise to the circuit. These modifications made the noise spectrum indistinguishable from the device noise floor, Figure 24. The scattered peaks vanished. A single, narrow resonance is evident around 3 MHz. However, we confirmed this peak to be coming from the measurement device itself.

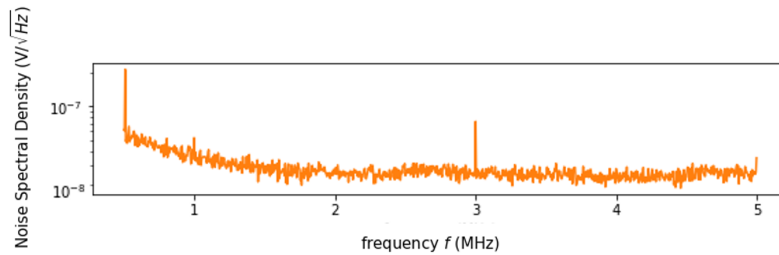


Figure 24: Noise spectral density at the OFB after moving the ground reference from the DAC power supply to an earthed copper pipe and removing the ground loop monitor is indistinguishable from the device noise floor. The resonance at 3 MHz originates at the measurement device.

The fact that the earthing changed the noise spectrum suggests that the culprit of these peaks is a noisy ground. Because those peaks are broad and large, we suspect this noise is picked up on the ground line of the mains ground. This could be through noisy devices connected to the mains ground line. A further investigation of the grounding configurations and their predicted heating rates will be carried out in Chapter 7.

5.3 RF Circuit Noise

Though we have likely determined the source of the observed scatter in one instance, we opted to look for other relevant sources and quantify their respective heating rates. This lets us know when and by what we would be limited next. The Johnson noise of the RF circuit can similarly be estimated through an electronic model of the full circuit including the noise of the RF source. A simplified schematic of the RF circuit can be seen in Figure 26.

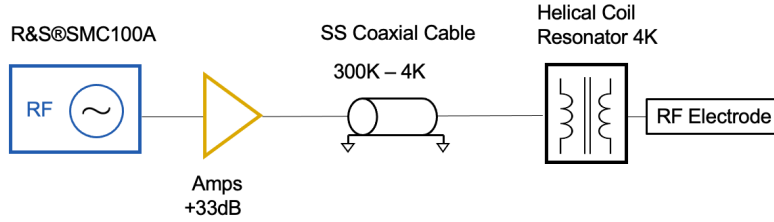


Figure 25: Simplified schematic of the RF circuit. An RF source generates a signal that is subsequently amplified. A stainless steel coaxial cable carries the signal to a helical coil resonator inside the 4K chamber, which allows signal amplification at the resonance frequency Ω_{RF} . The signal is carried to the electrode through wirebonds.

The wideband noise of the RF source can be extracted from the datasheet. Measurements of the source prior to this thesis showed insignificant dependence of the noise on the RF power. With the same procedure of noise propagation in the DC circuit, we can find the power noise spectral density on the RF electrodes, seen in Figure 26.

The noise spectral density is shown for frequencies up to 500 MHz. The first and most prominent peak corresponds to the voltage amplification through the helical coil resonator at the trap drive frequency Ω_{RF} . The subsequent peaks arise from short copper transmission lines further not depicted in the schematic. However, these are at higher frequencies than we care about. The RF circuit noise affects the ion when displaced from the RF null as the electric field in the radial direction becomes non-vanishing. The RF electrodes do not affect the axial direction since their axial field component is zero. The heating rate at frequency f from the RF circuit is computed using Equation (2.4) at frequency, in addition

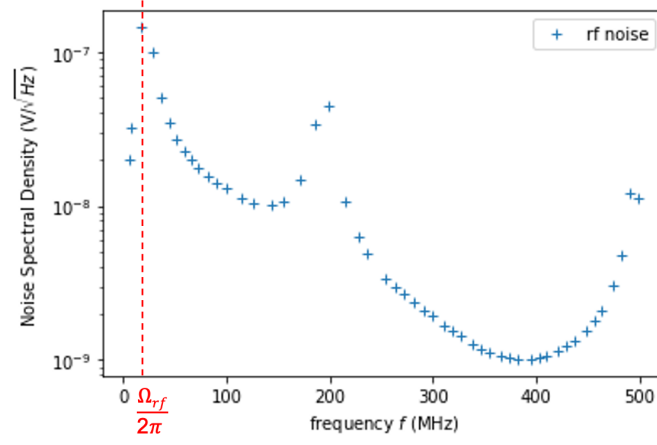


Figure 26: RF circuit power noise spectral density. The first peak at 20.6 MHz represents the amplification of the resonator at its fundamental resonant frequency. The lower peaks at 200 MHz and higher are resonances formed due to further transmission cables in the circuit (not shown in schematic).

to the modulated RF frequency contributions, Equation (2.5). The uncertainty in micromotion for the radials after implementing micromotion compensation is $\Delta y' \sim 20.3$ nm and $\Delta z' \sim 20.6$ nm. With an RF voltage of 183 V, the field gradient Φ''_{RF} in y' and z' can be obtained through the trap simulation. Figure 27 shows the resulting heating rates.

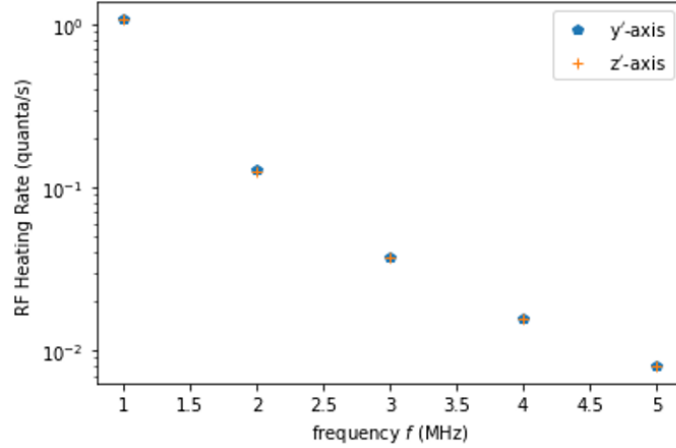


Figure 27: Expected heating rates of the RF circuit. Around the radial mode frequencies, the heating rate is on the order of 0.1 quanta/s. The RF circuit has no effect on the axial heating rate.

Around the radial frequencies (2–3 MHz), the RF noise would amount to heating rates on the order of 0.1 quanta/s; those heating rates are low enough to

perform fast gates without re-cooling. Moreover, measurements on the ion with displacement from the RF null up to $0.5 \mu\text{m}$ confirmed that the RF circuit had an insignificant influence on the heating rates.

5.3.1 SS vs Cu cable

The Dragonfly RF circuitry is identical to the PIEDMONS RF circuit. However, the heating rates in the Dragonfly trap were larger for modes more closely aligned with the direction pointing between the RF electrodes than between the DC electrodes. This could be explained by a differential noise on the opposing RF electrodes. In an attempt to symmetrize the radial heating rates, several modifications were implemented⁴. The heating rates were subsequently reduced by a factor of 20 and lost the polarization. One of the changes was the replacement of the stainless steel⁵ (SS) transmission line cable with a copper⁶ (Cu) transmission line. We simulate the noise of the RF circuit in the PIEDMONS trap with the Cu transmission line to quantify this cable's effect. Although Cu has a higher thermal conductivity than SS, its lower resistance⁷ allows for better signal transmission to the electrodes. We replace the R, L, and C values⁸ of the transmission line model in the circuit with Cu and plot the expected heating rates for one of the radial modes, Figure 28. The higher circuit gain increases the heating rates relative to the heating rate from the SS cable. However, the ratio of the Cu heating rates to SS is relatively small ~ 1.8 . Moreover, this modification cannot explain the polarization change in the heating rates. This will be revisited in Chapter 7.

5.4 Electromagnetic Pickup Noise

So far, we have seen how complicated and extensive cryogenic setups are. The forming of conductive loops within such setups is inevitable. Loops formed by unshielded lengthy voltage lines are subject to environmental magnetic field noise. The FFC cables in the DC circuit that carry the DC voltages from the outer filterboard at 300 K to the cryogenic filterboard at 4 K are ~ 76 cm in length. The FFC cables carry 51 lines. If we suppose that one of the lines leading to the electrodes forms a loop, we can predict the heating rates resulting from pickup noise in the system.

We obtain the magnetic field noise in the environment by forming a loop with

⁴See [24]

⁵Coax Co., Ltd. SC-086/50-SS-SS

⁶Coax Co., Ltd. SC-086/50-O-CN

⁷SS: $\rho = 6.9 * 10^{-7} \Omega\text{m}$ vs Cu: $\rho = 1.68 * 10^{-8} \Omega\text{m}$ at 20°C

⁸R, L, and C are per unit length (distributed-element model).

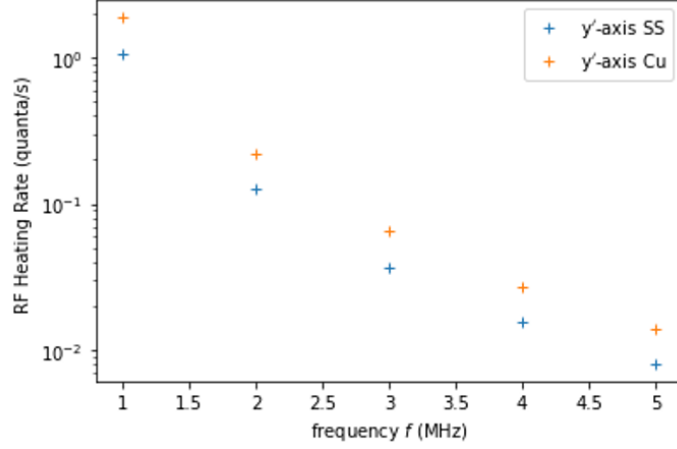


Figure 28: Expected y' heating rate of rf circuit with stainless steel SS (blue crosses) vs. copper Cu (orange crosses) transmission line. Cu possesses a lower resistance than SS, and the circuit's gain is higher.

area, A_L , and measuring the power noise spectral density around the cryostat ⁹. The orientation of the loop is chosen such that we obtain the largest noise. We translate the measured voltage noise into field through Equation (2.6). For the worst-case scenario, we assume a loop between the line leading to the electrode with the largest moment and the ground line. This allows a relatively larger loop area due to the distance of the ground line to the electrode line. We further suppose that the measured field is homogeneous and normal to the FFC wire. The last 15 cm of the FFC cables is within the 4K chamber. The 4K chamber is made of oxygen-free high-thermal conductivity copper (OFHC) and relatively thick ~ 18 mm. We can therefore see the 4K chamber as a Faraday cage suppressing magnetic field noise and include its shielding effects in our calculations. While the exact calculation of the suppression is complicated, without resorting to finite element modeling, we could assume a simple geometry of a spherical shell with electrical conductivity σ , magnetic permeability μ_r , radius r_0 and thickness $\Delta \ll r_0$. The field on the inside of this spherical shell is attenuated by [30]

$$\gamma \approx \frac{3\sqrt{2}\mu_r\delta}{r_0} e^{-\delta/\Delta} \quad (5.1)$$

where $\delta = \sqrt{2/\omega\mu_r\sigma}$ is the skin depth of the material. Equation (5.1) is valid in the limit of $\Delta, r_0 \gg \delta$.

With the linearity of the magnetic field, the induced voltage fluctuations along the separate areas of the loop can be calculated. To obtain the voltage noise of

⁹measurements showed insignificant changes to the signal at different positions around the setup.

those fluctuations at the trap electrode, we need to take the electronic model of this loop into consideration, i.e. the induced voltage is filtered through the cryogenic RC filter. With Equations (2.8) and (2.4), we convert the power noise spectral density into heating rates, seen in Figure 29.

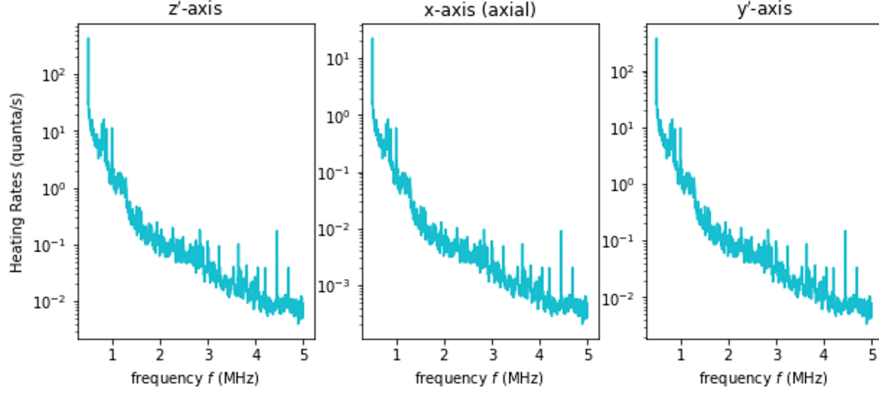


Figure 29: Expected worst-case heating rates of electromagnetic pickup noise along FFC cables based on a measurement of external field noise. Heating rates ~ 0.1 quanta/s for typical motional frequency modes.

For the frequency ranges where we typically position the motional modes, we expect relatively low heating rates of 0.1 quanta/s. We conclude that the pickup on the FFC lines is not a dominant noise source in the system. The heating rates based on external field noise measurements in Figure 29 are primarily due to the pickup on the FFC cables outside the 4K chamber, as most of the length is found outside. If these FFC cables were longer, $\sim 200\text{--}300$ cm, pickup noise would become a dominant factor in the setup with heating rates around 10–100 quanta/s. Shielded FFC cables present an easy solution to suppress the noise in cases where pickup noise could become limiting. These have since replaced the homemade manganin wires used in the Dragonfly setup (3.2.2).

5.5 Noise in the Dragonfly Trap

Heating rate characterization of the Dragonfly trap was performed in [15, 24]. The measurements were taken with the ion placed in the first experimental zone of the trap. Radial heating rate measurements were around ~ 1000 quanta/s at 4.4 MHz and displayed a noise polarization along the mode aligned between the RF electrodes, which we refer to as the RF diagonals. This could be explained by differential noise on the RF electrodes. Displacement of the ion along the RF diagonals did not affect the heating rates suggesting that the noise originates somewhere other than the RF circuit. Several setup modifications were subse-

quently implemented and observed to reduce heating rates¹⁰. Figure 30 shows a plot of the measured heating rates vs. frequency for the radial modes after modifications.

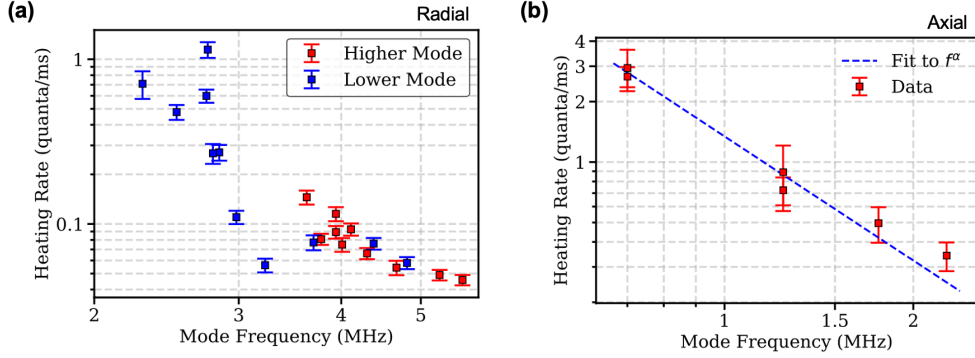


Figure 30: Measured heating rates vs. frequency f . (a) The radials are tilted by $\theta = 40.5^\circ$ from the xz -plane, with the higher frequency mode pointing along the RF diagonals and the lower frequency pointing along the direction between the DC electrodes. Heating rates reach ~ 80 quanta/s around 4 MHz. (b) Axial heating rates with exponent fit $\alpha = -2.05$. Axial heating rates are higher than radial modes. Temperature insensitivity suggests technical noise. Taken from [15].

The higher frequency mode in Figure 30 (a) corresponds to the mode along the RF diagonals, y' , while the lower frequency mode points along the DC diagonals. This configuration is achieved by tilting $\theta = 40.5^\circ$ from the xz -plane. The heating rates appeared to have lost their polarization and were reduced to ~ 80 quanta/s. Furthermore, the heating rates increase rapidly with lower mode frequencies. The axial heating rates, Figure 30 (b), are much higher than the radial heating rates. Investigations showed a weak correlation between the trap temperature with the axial heating rate suggesting an external noise source. Speculations of external noise via the DC circuit were raised [15]. This section will therefore attempt to model the Dragonfly DC circuit noise and its expected heating rates and compare them to the PIEDMONS' heating rates.

We perform noise spectral density measurements at the OFB (Figure 8 (a)) and propagate the measured noise onto the DC electrodes. Since the ion is typically trapped in the first experimental zone of the trap, only the first 20 DC electrodes on the top and bottom wafers are considered. Considering Johnson noise of the circuit components for each electrode voltage line, we assume no correlation of the noise on different electrodes. Expected heating rates can be seen in Figure 31. The OFB measurement results are indistinguishable from the

¹⁰Modifications listed in [15]

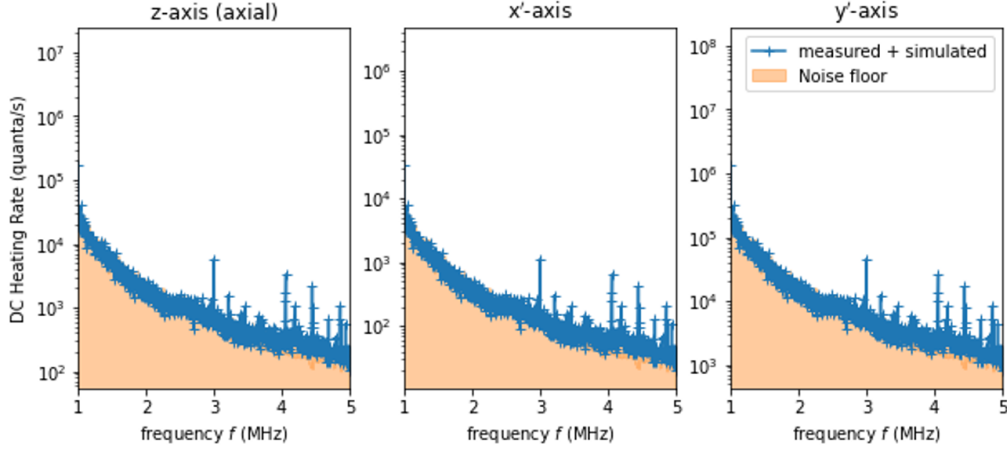


Figure 31: Expected heating rates of outer filterboard measurement (blue traces). The radials are tilted by $\theta = 40.5^\circ$ from xz -plane. Predicted heating rates [based on propagation of the device noise floor] are higher than those measured, suggesting that external measurements with this device are not sensitive enough to detect limiting technical noise sources.

measurement device’s noise floor. Narrow resonances are present around 3–5 MHz. Due to their narrow shape, we suspect they are possibly due to digital switching within devices found in the laboratory and could likely be picked up by the measurement cables or originate in the digital circuitry of the DEATH board supplying the voltages (see Section 3.2.2). By propagating this measured noise forward we consider a worst-case scenario as the noise of the DC circuit is presumably lower than the measurement devices’ noise floor. The predicted heating rates in Figure 30 are at least an order of magnitude higher than the measured rates on the ion, Figure 30. This suggests that the input noise within the Dragonfly trap at the OFB is lower relative to the noise floor.

For the PIEDMONS trap, the same device noise floor would amount to lower heating rates. This is due to stronger cryogenic filtering. Moreover, 11 electrodes contribute noise within the PIEDMONS setup, whereas the Dragonfly trap includes the noise of 20 electrodes.

Figure 31 shows an asymmetry in the heating rates with higher heating in the y direction along the RF electrodes. Such an observation has been made with measured heating rates on the ion before setup modifications, details in [16]. This asymmetry could hint at noise coupled to the ion through the DC circuit. Nevertheless, the exact noise source leading to the measured heating rates after modifications (Figure 30) requires further characterization. We will refer to this observation in Chapter 7.

Noise Models

6.1 Independent vs Common Mode Noise

There are many signal paths through which noise can reach the ion. This noise can be common, such as if it is generated at a distant source, and partially travels along each of these paths in a related manner. Or, independent noise sources could exist along each path. These different scenarios can produce signatures at the ion, affecting heating rate levels and geometry-dependent noise polarization. By understanding these models and the signatures they can produce, we can pinpoint the type of noise source that is responsible.

In Section 5.2, we assumed the noise on different electrodes was uncorrelated, a type of noise we will term “independent”. The heating rate is proportional to the sum of the electric field fluctuations on each electrode:

$$S_E = \sum_i S_V \kappa_i^2, \quad (6.1)$$

where κ_i is the moment of electrode i along the direction of interest. This model describes the case, for example, in which Johnson noise originates in the filter electronics on each line. The noise magnitude on all electrodes is the same and has no fixed phase relation.

When noise originates in a shared line such as the ground line as we have characterized in section 5.2.1, the noise would be “common” to all electrodes. This means the noise is entirely correlated, and the heating rate is proportional to the noise of the resulting moment of all electrodes, i.e.

$$S_E = S_V \left(\sum_i \kappa_i \right)^2. \quad (6.2)$$

Reviewing the analysis for the DC circuit with a common mode noise model rather than the independent noise source, we obtain the heating rates seen in Figure 32.

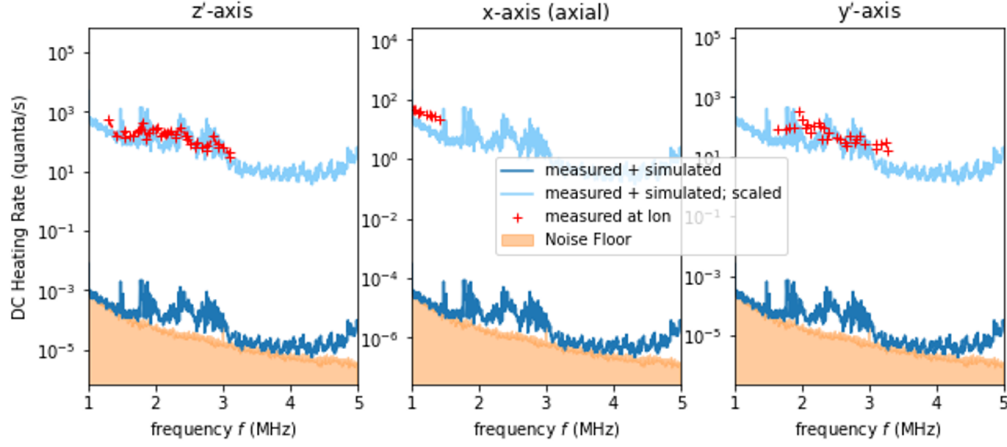


Figure 32: Expected heating rates (blue) from the OFB with a common mode noise model. The radials are tilted by 38° from xy -plane. Measured heating rates (red crosses) are ~ 6 orders of magnitude higher. The light blue trace represents the blue trace scaled by $10^{5.8}$ to match the measured rates.

The expected heating rates (blue traces) with common mode noise do not meet the level of the measured heating rates. If our electronic model fails to capture an element that could scale the expected common mode noise in such a way as to match the measured values, the common mode noise model could not be ruled out. The expected heating rates would need to be scaled by 5.8 orders of magnitude (light blue trace) to match the scatter in the radials. However, considering reasonable uncertainty of circuit parameters, we cannot justify such scaling.

To note is that while the z-axis independent model trace would match the heating rate trace of the scaled common mode (Figure 33), the ratio of both rates for the y-axis is ~ 2.5 . This is most likely due to the nature of the noise models. With the independent noise modes, the magnitudes of the moments determine the dominant terms, while in the common mode noise the symmetry of the trap determines the noise orientation. Between 2 and 2.5 MHz, the measured red crosses match with the independent model rates, whereas above 2.5 MHz, they are within the values expected for both the common and independent noise model.

6.2 Noise Polarization Ratio

To visualize the difference between both models in terms of heating rates, we define the “noise polarization ratio”, R , as

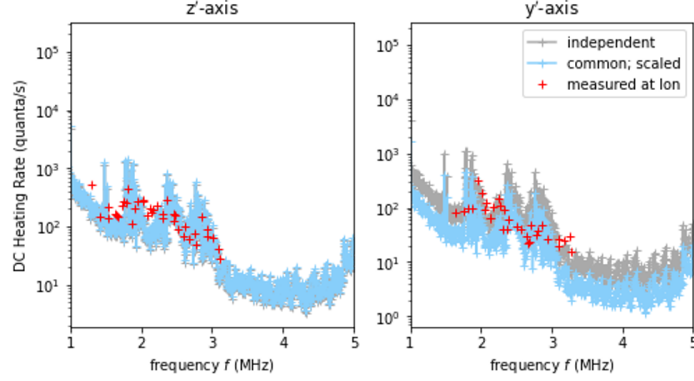


Figure 33: Comparison of the expected heating rates in the PIEDOMONS trap from independent noise (grey) vs. common noise scaled by $10^{5.8}$ (light blue). The heating rates of the z' mode match, while a factor of 2.5 separates the independent rates from the scaled common modes in the y' mode.

$$R = \frac{S_E \text{ along } y'}{S_E \text{ along } z'}. \quad (6.3)$$

That is, the ratio of the heating rate in the in-plane direction (y' -axis) to the out-of-plane direction (z' -axis). The PIEDOMONS trap is fully symmetric in the x - and y -axis as shown in Figure 5 (b). This geometry would result in only a non-zero field along the z -coordinate when summing the field created by all electrodes. Therefore, when the radial modes are tilted by 45° from the xy -plane, we expect the heating rates to match, i.e., $R = 1$.

Small misalignments in the trap could result in a field with a non-zero projection in the y -coordinate. The independent noise model would not be affected by such small misalignments as the dominant contributions come from the largest electrode moments; calculations predict a ratio of ~ 1 at 45° from the xy -plane. Meanwhile, common mode noise is susceptible to such misalignment. The point at which the radial rates meet is set at 45° from the angle of the total electric field of all electrodes. For instance, due to numerical errors in the simulation, the total residual electric field forms an angle $\alpha = 8.4^\circ$ from the z -axis. Calculations find the ratio to be ~ 1 at $45^\circ + 8.4^\circ$. Numerical simulations are typically relatively accurate to $\leq 10\%$ and real trap imperfections are expected to be much larger forming a larger angle with the z -axis.

In Figure 34, heating rates vs. mode angle ϕ from the xy -plane are plotted. For the predicted common and independent noise model heating rates, the in-plane modes are plotted for $0 \leq \phi \leq 45$ while the out-of-plane mode heating

rates are plotted for $45 \leq \phi \leq 90$. In terms of heating rates, the common mode noise would result in a discontinuity at 45° from the xy -plane while the independent noise model would be continuous at this angle. The measured heating rates (red) are plotted and fitted to a sinusoidal function. Towards 45° , spectral resolution becomes challenging since the trap geometry forces the modes to become degenerate [31].

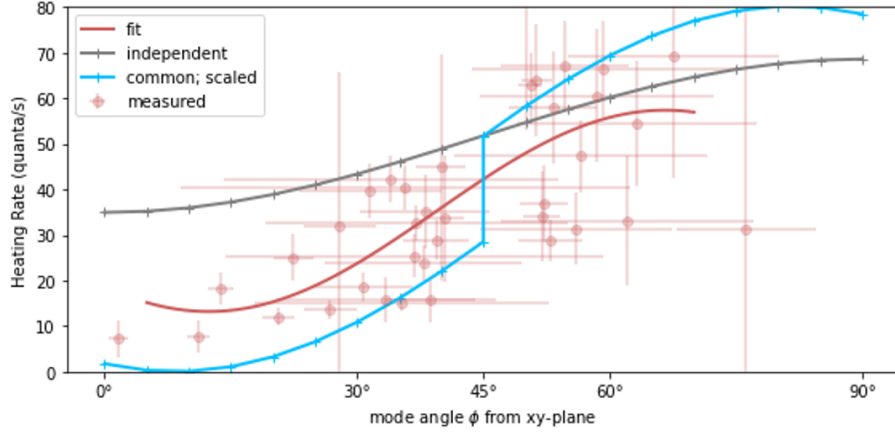


Figure 34: Heating rates vs mode angle ϕ from xy -plane. Measured values (red circles) could be fitted to a sine curve. Within the error bars, the measured heating rate curve is continuous around 45° . Grey and light blue curves show the expected heating rate vs mode angle curve from independent vs. common mode noise model. The common mode heating rate is discontinuous at 45° due to simulated trap misalignments. Below $\sim 30^\circ$, the heating rates drop relatively lower than expected in the independent noise model.

While the fit of the measured heating rates seems to suggest that the radial heating rates meet around 45° , and within the uncertainty points to match with the independent noise model trace (grey), the fit does not allow for a discontinuity. Moreover, below $\sim 30^\circ$, the drop in the heating rates is closer to that seen in the common mode noise (light blue). We conclude that the noise model is a mixture between common mode and independent. One theoretical explanation could be that the DAC ground reference differs from the trap ground because of non-negligible resistance between them. The point at which this change can happen within the setup is hard to track down. The worst-case scenario, i.e., independent noise, is typically adopted for the noise correlation of electrodes in such complex setups.

Modifications and Recent Heating Rates

In Chapter 5, we attempted to find the noise source that dominantly limits the heating rates of the PIEDMONS trap. Noise measurement results suggest that the systems ground reference is noisy. To verify this, we perform heating rate measurements with different grounding configurations and look for the optimal configuration that reduces the heating rates of the system.

7.1 Measured Heating Rates vs. Setup Configurations

At the start of the thesis, the PIEDMONS setup was partially disassembled. While reassembling the setup, we replaced the SS coaxial cable in the RF circuit with a Cu cable. Although we have shown that, in theory, this modification has a negligible effect on the heating rates, the Cu cable offers better thermalization. It is hence beneficial for connections between the source at room temperature (300K) and the resonator at the 4K stage. Moreover, the power supply to the Ground Loop Monitor (Figure 11) has been replaced as it was observed to add noise to the system. With the system ready to be operated, the ion can be used to verify if the ground reference of the system is the limiting noise source for the radial modes.

As a preliminary evaluation, we measure the radial heating rates for different grounding configurations at frequencies of 2.1 MHz and 2.4 MHz for the in- and out-of-plane direction, respectively. The radial modes are rotated by an angle of 38° relative to the xy -plane with a trap temperature ~ 10 – 40 K. The measurement results are plotted in Figure 35. Configuration (i) corresponds to the same grounding configuration as in the previously measured heating rates, shown in Figure 18. This is where the ground is referenced to the DAC power supply, which is earthed by the mains ground. In Section 5.2.1, we have seen that the noise spectrum in this configuration exhibits peaks around the typical radial frequencies that match the scatter observed in the measured heating rates. By switching the ground reference to an earthed Cu pipe, these noise peaks were

not visible anymore. The measured heating rates with this modification is shown in configuration (ii). Surprisingly, Figure 35 shows lower heating rates to the initial grounding configuration, configuration (i), in comparison to the modified configuration, configuration (ii).

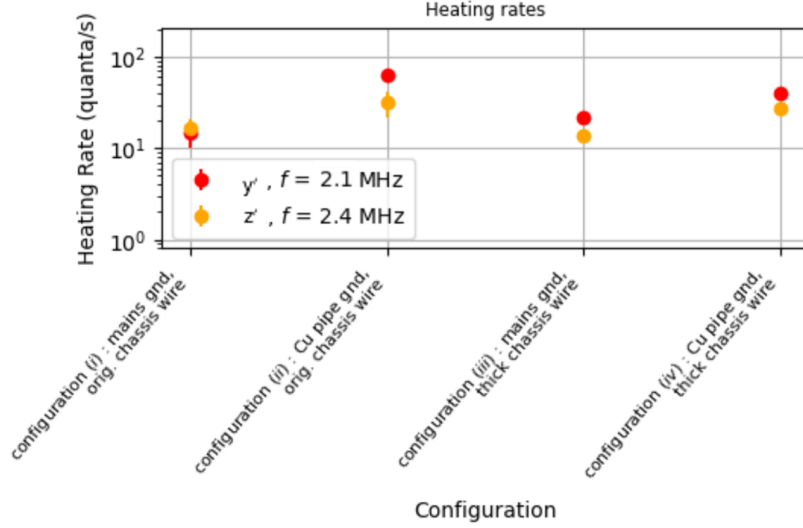


Figure 35: Heating rates vs grounding configuration for the in- (y') and out-of-plane modes (z') at frequencies 2.1 MHz and 2.4 MHz, respectively. The radial modes are rotated by an angle of 38° relative to the xy -plane. Configurations (i) and (iii) correspond to the grounding configuration with the ground referenced to the mains ground through the DAC power supply, whereas, configurations (ii) and (iv) correspond to the grounding referenced to an earthed Cu pipe. Configurations (iii) and (iv) include an additional thick wire connecting the DAC ground line to the cryostat.

In Chapter 3, we mentioned that a chassis grounding arrangement is chosen. This is carried out in the setup through a thin jumper wire connecting the signal ground lines on the OFB to the cryostat. The grounding can further be improved by adding another wire connecting the DAC ground to the cryostat. This enhances the effect of the chassis grounding to avoid large ground loops. Moreover, since the noise originates at an earlier point in the circuit (the ground line) by connecting the ground directly to the cryostat, PCB-to-PCB connections are bypassed. This configuration leads to a lower probability of the noise propagating through the filters. We choose a thick wire to ensure a low-impedance path to the cryostat. Configurations (iii) and (iv) in Figure 35 correspond with the ground reference as in configurations (iii) and (iv), respectively, with the additional thick wire connecting the DAC ground to the cryostat. The effect of the thick wire on the grounding configurations seems to have little impact on the heating rates. For further measurements of heating rates, we will proceed with configura-

tions (*iii*) and (*iv*) for the benefits of enhancing a chassis grounding arrangement.

To compare the effect of the setup modifications and the different grounding configurations to the previously seen heating rates in Figure 18, we measure the radial heating rates as a function of frequency. The radial frequencies can be varied with the RF voltage. For each RF voltage, the radial frequency is identified through carrier spectroscopy and sideband transitions [24] and micromotion compensation is implemented. Following cooling calibrations, heating rates are measured through sideband cooling as discussed in Chapter 2. Figure 36 shows the measured radial heating rates as a function of frequency. The setup for (a) is the one described in the previous chapters with no modifications and is equivalent to Figure 18 (a). (b) is equal to configuration (*iii*) i.e., the modified setup with the ground referenced to the mains ground through the DAC power supply as in (a). The configuration in (c) corresponds to the modified setup with the ground referenced to an earthed Cu pipe as in (*iv*). With the new set of measured heating rates, the trap temperature was $\sim 10\text{--}40$ K, which is much lower compared to the previous measurement, Figure 18, where the trap temperature reached ~ 185 K. For comparison, data points in Figure 36 (a) have been normalized to a temperature ~ 10 K.

For plots with the ground referenced to the mains ground, as in Figure 36 (a) and (b), the heating rates of the modified setup, Figure 36 (b), exhibit scatter on a lower level. This could be attributed to the additional thick wire enhancing the chassis grounding arrangement. However, since we suspect that the scatter is noise picked up on the ground line of the mains ground. It is also likely to have generally less noise in the ground line through fewer connections/disconnections of noisy devices to the mains ground of the building. The level of the heating in both plots is nevertheless comparable. By earthing through the Cu pipe, the heating rates are reduced by almost an order of magnitude and follows a different trend as seen in Figure 36 (c). A scatter behaviour is obvious, however at lower frequencies, and could be related to temporal changes on the Cu pipe. The change in the trend of the scatter and the reduction of the heating rates by changing the grounding configuration confirm the suspicion raised in the previous chapters of noise in the ground line propagating to the ion. Thereby verifying the method proposed for source characterization of noise based on heating rate measurements.

In comparison to the previously non-modified setup, the heating rates in Figure 36 (b) and (c) seem to have lost the polarisation. In Figure 36 (a), a clear gap is present between the heating rates of the in- (yellow points) and out-of-plane modes (red points), with the out-of-plane heating rates higher by an average factor of ~ 2.8 . Figure 36 (b) and (c) show no such gap. The heating rates for in- and out-of-plane orientations always meet within the error bars. Such an observation of lost polarization has been made in the Dragonfly setup after

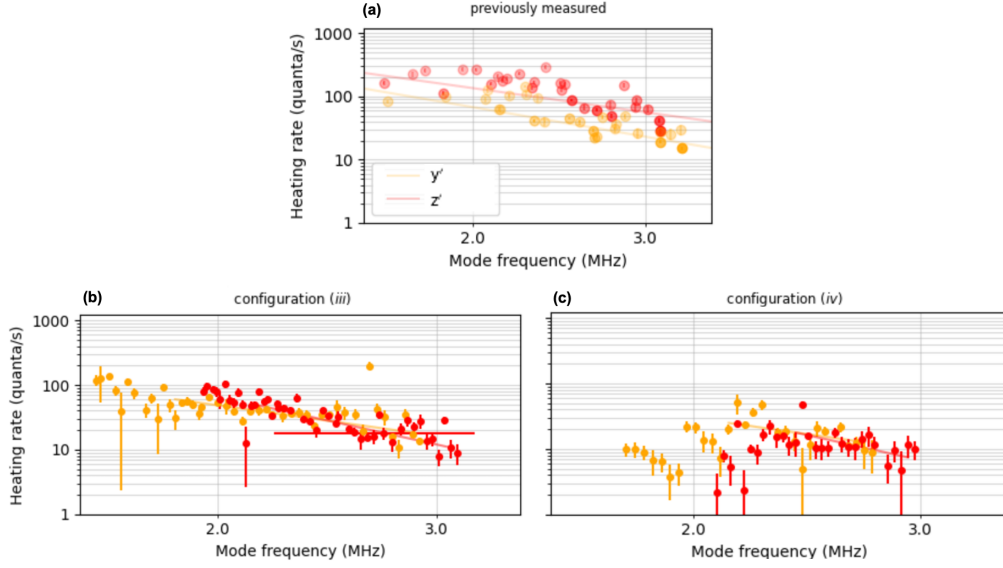


Figure 36: Radial heating rates vs frequency for three different configurations. The radial modes are rotated by an angle of 38° relative to the xy -plane. (a) The measured values correspond to the previously data plotted in Figure 18 (a). The setup configuration is as previously described with the ground earthed to the mains ground through the DAC power supply. Configurations (b) and (c) represent the newly measured heating rates after the replacement of the Cu cable with a SS cable in the RF circuit and an additional thick wire connecting the DAC ground to the cryostat. The earth is referenced to the mains ground through the DAC power supply in (b) whereas the ground is earthed to a Cu pipe in (c).

certain modifications, Section 5.5. The one common modification present in both setups, PIEDMONS and Dragonfly, is the replacement of the SS coaxial cable in the RF circuit to a Cu coaxial cable. In Section 5.3, we have shown that this replacement has little to almost no impact on the heating rates. However, our model does not take into account noise that could be present on the ground line of the coaxial cable. Suppose some noise is present on the ground line of the cable, the higher resistance of the SS cable would cause a large voltage drop. This does not clarify the polarization of the noise in a specific mode direction. Coupling of the ground noise in the RF circuit to the DC circuit through a shared ground plane at the trap could result in asymmetry of the noise. This would depend on the type of coupling into the DC electrodes and the symmetry of the trap. For a detailed explanation of the mechanism and verification of the hypothesis, further analysis would need to be carried out.

Conclusion and Outlook

A method for modeling heating rates from various external noise sources was developed through technical concepts and noise measurements with a spectrum analyzer. Comparison of modeled vs. measured heating rates of the PIEDMONS trap helped identify the DC circuit as dominantly limiting the radial heating rates. Considerations of heating through other external sources, such as the RF circuit and electromagnetic pickup, were considered to know when they could become limiting. This was found to be around 0.1 quanta/s, three orders of magnitude lower than the initially measured heating rates of the trap [14]. The noise source was found to be a noisy mains ground line through repeated noise measurements with different filters and grounding configurations. Since the mains ground is a central ground for the entire building with many device connections, it is highly likely to be picked-up noise from noisy devices. Through playing with the grounding configuration, a cleaner noise spectrum was achieved by grounding to an earthed Cu pipe in the lab. However, the measurement was limited by the noise floor of our measurement device, FieldFox RF Analyzer N9912A, with ~ 40 nV/ $\sqrt{\text{Hz}}$. The high noise floor of the device was as well the issue encountered when attempting to model the DC circuit noise for the Dragonfly trap. Therefore we were unsuccessful with modeling the DC noise and no further noise source characterization on the Dragonfly trap was attempted. Characterization of the measurement device with a preamplifier revealed that below 2 MHz, the device is not reliable. Hence, for future measurements around 0.5–2 MHz and with noise lower than ~ 80 – 100 nV/ $\sqrt{\text{Hz}}$, which is the typical noise floor of oscilloscopes used in our labs, an oscilloscope with the use of a preamplifier is the more reliable option for noise measurements.

When modeling the heating rates resulting from noise on the DC electrodes, the correlation of the noise between different electrodes has to be considered. The nature of the noise source determines this. We analyze the case of independent, uncorrelated noise vs. common mode, maximally correlated noise. We initially argue that a noisy ground line would lead to a common mode noise behavior due to the ground being shared by all electrodes. However, the predicted heating rate level from common mode noise is six orders of magnitude lower than the measured heating rates. Moreover, the behavior of the heating rates as a function of mode angle suggests that the noise is a mixture between a common mode and an

independent model. With the complexity of the setup, many factors could play a role in the correlation of the noise. Hence, the worst-case model, independent noise, should typically be assumed.

We verified the predicted effect of the ground reference based on noise measurements by performing heating rate measurements on the ion for different grounding configurations. The setup underwent modifications since the measured heating rates we attempted to model. A SS coaxial cable in the RF circuit was switched to a Cu cable for better thermalization, and a thick wire connecting the DAC output to the cryostat was added to enhance the chassis ground arrangement. The measurements show that the heating rate levels were lower by almost an order of magnitude, with the ground referenced to the Cu pipe rather than to the mains ground. The new measurements revealed a much lower scatter for the Cu pipe and the mains ground reference. This could be attributed to changes in the noise of the ground line or the additional thick wire. Moreover, the new measurements exhibit no polarization of the noise. This was the same observation as in the Dragonfly trap after modifying the setup. The common modification to both setups is the replacement of the SS cable with Cu in the RF circuit. A theoretical explanation of the polarization loss could be through ground line noise in the RF circuit coupling into the DC circuit. The higher resistance of the SS cable would result in a higher voltage drop and, consequently more significant effect on the heating rates. The level of polarization is determined by the symmetry of the trap and the type of coupling present.

The main results of the thesis, along with a recent discovery by the Dragonfly setup that shows the ion's motional coherence to be strongly limited by the grounding configuration at times, lead to the conclusion that a good grounding configuration is essential for technically limited ion-trap setups, especially in terms of heating rates. However, a more detailed understanding of the grounding is necessary for more systematic enhancements to the setup and, in response, the heating rates of the system. For instance, although outside filters are placed between the DAC output and the trap, the noise on the ground line continues to propagate forward to the DC electrodes. Moreover, we have yet to understand the noise model regarding chassis vs. signal line grounding configuration. Before this thesis, the PIEDMONS and Dragonfly trap measured three orders of magnitude higher heating rates when the current return path was through signal lines. Intuitively, a higher resistance path to the ground through the signal lines would cause more significant voltage drops instead of connecting the grounds at multiple points to the metal of the cryostat with less resistance. However, noise currents need to be included to quantify the effect, which is typically challenging to model.

As a next step towards improving the setup, a Fastino DAC board [32] will replace the current DAC, AD5371. This offers a faster voltage update rate bene-

ficinal for ion transport experiments. The output noise of the Fastino, along with its amplifier board, is $\sim 4 \text{ nV}/\sqrt{\text{Hz}}$. This should result in a heating rate of 0.1 quanta/s. Moreover, the Fastino setup is much simpler than the DC circuit since it is placed along with the filters needed inside an electronic rack. One single connector PCB will deliver the voltages to the trap. Additional filters could potentially be used if the noise is much higher than anticipated. The Fastino is in high demand for several setups in our group. Therefore, measured heating rates with the Fastino would serve as a performance indicator.

Bibliography

- [1] J. A. Sedlacek, J. Stuart, W. Loh, R. McConnell, C. D. Bruzewicz, J. M. Sage, and J. Chiaverini, “Method for determination of technical noise contributions to ion motional heating,” in *Journal of Applied Physics*, vol. 124, p. 214904, 2018.
- [2] A. Y. Kitaev, “Quantum computations: algorithms and error correction,” in *Russian Mathematical Surveys*, vol. 52, pp. 1191-1249, 1997.
- [3] K. R. Brown, J. Chiaverini, J. M. Sage, and H. Haefner, “Materials challenges for trapped-ion quantum computers,” in *Nature Reviews Materials*, vol. 6, pp. 892-905, 2021.
- [4] J. I. Cirac and P. Zoller, “Quantum computations with cold trapped ions,” in *Physical Review A*, vol. 74, pp. 4091-4094, 1995.
- [5] A. Sørensen and K. Mølmer, “Entanglement and quantum computation with ions in thermal motion,” in *Physical Review A*, vol. 62, p. 022311, 2000.
- [6] C. Monroe, D. M. Meekhof, B. E. King, W. M. Itano, and D. J. Wineland, “Demonstration of a fundamental quantum logic gate,” in *Physical Review Letters*, vol. 75, pp. 4714-4717, 1995.
- [7] C. Monroe, D. M. Meekhof, B. E. King, S. R. Jefferts, W. M. Itano, D. J. Wineland, and P. Gould, “Resolved-sideband raman cooling of a bound atom to the 3d zero-point energy,” in *Physical Review Letters*, vol. 75, pp. 4011-4014, 1995.
- [8] D. M. Meekhof, C. Monroe, B. E. King, W. M. Itano, and D. J. Wineland, “Generation of nonclassical motional states of a trapped atom,” in *Physical Review Letters*, vol. 76, pp. 1796-1799, 1996.
- [9] C. Roos, T. Zeiger, H. Rohde, H. C. Nägerl, J. Eschner, D. Leibfried, F. Schmidt-Kaler, and R. Blatt, “Quantum state engineering on an optical transition and decoherence in a paul trap,” in *Physical Review Letters*, vol. 83, pp. 4713-4716, 1999.
- [10] B. E. King, C. S. Wood, C. J. Myatt, Q. A. Turchette, D. Leibfried, W. M. Itano, C. Monroe, and D. J. Wineland, “Cooling the collective motion of trapped ions to initialize a quantum register,” in *Physical Review Letters*, vol. 81, pp. 1525-1528, 1998.

- [11] Q. A. Turchette, C. S. Wood, B. E. King, C. J. Myatt, D. Leibfried, W. M. Itano, C. Monroe, and D. J. Wineland, “Deterministic entanglement of two trapped ions,” in *Physical Review Letters*, vol. 81, pp. 3631–3634, 1998.
- [12] J. Labaziewicz, Y. Ge, P. Antohi, D. Leibbrandt, K. R. Brown, and I. L. Chuang, “Suppression of heating rates in cryogenic surface-electrode ion traps,” in *Physical Review Letters*, vol. 100, p. 013001, 2008.
- [13] Q. A. Turchette, Kielpinski, B. E. King, D. Leibfried, D. M. Meekhof, C. J. Myatt, M. A. Rowe, C. A. Sackett, C. S. Wood, W. M. Itano, C. Monroe, and D. J. Wineland, “Heating of trapped ions from the quantum ground state,” in *Physical Review A*, vol. 61, p. 063418, 2000.
- [14] S. Auchter, C. Axline, C. Decaroli, M. Valentini, L. Purwin, R. Oswald, R. Matt, E. Aschauer, Y. Colombe, P. Holz, R. Blatt, P. Schindler, C. Rössler, and J. Home, “Industrially microfabricated ion trap with 1 ev trap depth,” in *Quantum Science and Technology*, vol. 71, p. 035015, 2022.
- [15] C. Decaroli, R. Matt, R. Oswald, M. Ernzer, J. Flannery, S. Ragg, and J. P. Home, “Design, fabrication and characterization of a micro-fabricated stacked-wafer segmented ion trap with two x-junctions,” in *Quantum Science and Technology*, vol. 6, p. 044001, 2021.
- [16] R. B. Blakestad, C. Ospelkaus, A. P. VanDevender, J. M. Amini, J. Britton, D. Leibfried, and D. J. Wineland, “High-fidelity transport of trapped-ion qubits through an x-junction trap array,” in *Physical Review Letters*, vol. 102, p. 153002, 2009.
- [17] R. B. Blakestad, a. A. P. V. C. Ospelkaus, J. H. Wesenberg, M. J. Biercuk, D. Leibfried, and D. J. Wineland, “Near-ground-state transport of trapped-ion qubits through a multidimensional array,” in *Physical Review A*, vol. 84, p. 032314, 2011.
- [18] M. Brownnutt, M. Kumph, P. Rabl, and R. Blatt, “Ion-trap measurements of electric-field noise near surfaces,” in *Reviews of Modern Physics*, vol. 87, pp. 1419–1482, 2015.
- [19] D. J. Wineland, C. Monroe, W. M. Itano, B. E. King, D. Leibfried, D. M. Meekhof, C. Myatt, and C. Wood, “Experimental primer on the trapped ion quantum computer,” in *Fortschritte der Physik*, vol. 46, pp. 363–390, 1998.
- [20] L. Deslauriers, P. C. Haljan, P. J. Lee, K.-A. Brickman, B. B. Blinov, M. J. Madsen, and C. Monroe, “Zero-point cooling and low heating of trapped 111cd^+ ions,” in *Physical Review A*, vol. 70, p. 043408, 2004.
- [21] D. A. Hite, Y. Colombe, A. C. Wilson, K. R. Brown, U. Warring, R. Jördens, J. D. Jost, K. S. McKay, D. P. Pappas, D. Leibfried, and D. J. Wineland,

- “100-fold reduction of electric-field noise in an ion trap cleaned with in situ argon-ion-beam bombardment,” in *Physical Review Letters*, vol. 109, p. 103001, 2012.
- [22] D. Hite, Y. Colombe, A. Wilson, D. Allcock, D. Leibfried, D. Wineland, and D. Pappas, “Surface science for improved ion traps,” in *Mrs Bulletin*, vol. 38, pp. 826-833, 2013.
- [23] J. B. Johnson, “Thermal agitation of electricity in conductors,” in *Physical Review*, vol. 32, pp. 97-109, 1928.
- [24] C. Decaroli, “*Multi-wafer ion traps for scalable quantum information processing.*” PhD thesis, ETH Zurich, 2021.
- [25] R. J. Epstein, S. Seidelin, D. Leibfried, J. H. Wesenberg, J. J. Bollinger, J. M. Amini, R. B. Blakestad, J. Britton, J. P. Home, W. M. Itano, J. D. Jost, E. Knill, C. Langer, R. Ozeri, N. Shiga, and D. J. Wineland, “Simplified motional heating rate measurements of trapped ions,” in *Physical Review A*, vol. 76, p. 033411, 2007.
- [26] J. H. Wesenberg, R. J. Epstein, D. Leibfried, R. B. Blakestad, J. Britton, J. P. Home, W. M. Itano, J. D. Jost, E. Knill, C. Langer, R. Ozeri, S. Seidelin, and D. J. Wineland, “Fluorescence during doppler cooling of a single trapped atom,” in *Physical Review A*, vol. 76, p. 053416, 2007.
- [27] V. Negnevitsky, “*Feedback-stabilised quantum states in a mixed-species ion system.*” PhD thesis, ETH Zurich, 2018.
- [28] K. Nesterov, “*Development of an RF resonator for a double junction ion trap.*” Semester thesis, ETH Zurich, 2019.
- [29] M. Kumph, C. Henkel, P. Rabl, M. Brownnutt, and R. Blatt, “Electric-field noise above a thin dielectric layer on metal electrodes,” in *New Journal of Physics*, vol. 18, p. 023020, 2016.
- [30] S. Celozzi, R. Araneo, and G. Lovat, *Electromagnetic Shielding*. Wiley Series in Microwave and Optical Engineering. Hoboken, NJ, USA: John Wiley Sons, Inc., 2008, pp. pp. 282–291.
- [31] J. Amini, J. Britton, D. Leibfried, and D. Wineland, *Microfabricated Chip Traps for Ions*. Atom Chips, WILEY-VCH Verlag, Weinheim, -1, 2011-04-12 2011.
- [32] M. Marti, “*Low-Noise DC Amplifier Design for Trapped Ion Setups Bayesian Schemes for Fast Single Qubit Detection.*” Master thesis, ETH Zurich, 2022.



Eigenständigkeitserklärung

Die unterzeichnete Eigenständigkeitserklärung ist Bestandteil jeder während des Studiums verfassten Semester-, Bachelor- und Master-Arbeit oder anderen Abschlussarbeit (auch der jeweils elektronischen Version).

Die Dozentinnen und Dozenten können auch für andere bei ihnen verfasste schriftliche Arbeiten eine Eigenständigkeitserklärung verlangen.

Ich bestätige, die vorliegende Arbeit selbständig und in eigenen Worten verfasst zu haben. Davon ausgenommen sind sprachliche und inhaltliche Korrekturvorschläge durch die Betreuer und Betreuerinnen der Arbeit.

Titel der Arbeit (in Druckschrift):

Identifying Limiting Noise Sources in Cryogenic Ion-Trap Systems

Verfasst von (in Druckschrift):

Bei Gruppenarbeiten sind die Namen aller Verfasserinnen und Verfasser erforderlich.

Name(n):

Mashaal

Vorname(n):

Aida

Ich bestätige mit meiner Unterschrift:

- Ich habe keine im Merkblatt [„Zitier-Knigge“](#) beschriebene Form des Plagiats begangen.
- Ich habe alle Methoden, Daten und Arbeitsabläufe wahrheitsgetreu dokumentiert.
- Ich habe keine Daten manipuliert.
- Ich habe alle Personen erwähnt, welche die Arbeit wesentlich unterstützt haben.

Ich nehme zur Kenntnis, dass die Arbeit mit elektronischen Hilfsmitteln auf Plagiate überprüft werden kann.

Ort, Datum

Zürich, 23.11.2022

Unterschrift(en)

Bei Gruppenarbeiten sind die Namen aller Verfasserinnen und Verfasser erforderlich. Durch die Unterschriften bürgen sie gemeinsam für den gesamten Inhalt dieser schriftlichen Arbeit.